Golgi derived PI(4)P-containing vesicle drives late steps of mitochondrial division*

Short Title: PI(4)P regulates mitochondrial fission

One sentence summary: Golgi-derived vesicles loaded with the specific lipid PI(4)P contribute to the final steps of mitochondrial division

Shun Nagashima[1], Luis-Carlos Tábara[1†], Lisa Tilokani[1†], Vincent Paupe[1], Hanish Anand[1], Joe H. Pogson[2], Rodolfo Zunino[2], Heidi M. McBride[2*] and Julien Prudent[1*]

[1.] Medical Research Council Mitochondrial Biology Unit, University of Cambridge, Cambridge Biomedical Campus, Hills Road, Cambridge, CB2 0XY, United Kingdom.

[2.] Department of Neurology and Neurosurgery, McGill University, 3801 University Avenue, Montreal, Quebec, H3B 2B4, Canada.

[†] These authors contributed equally

[*] To whom correspondence be addressed:

Emails: Heidi.mcbride@mcgill.ca; Julien.prudent@mrc-mbu.cam.ac.uk

ABSTRACT

Mitochondrial plasticity is a key regulator of cell fate decisions. Mitochondrial division involves Dynamin-related protein-1 (Drp1) oligomerization, which constricts membranes at endoplasmic reticulum (ER) contact sites. The mechanisms driving the final steps of mitochondrial division are still unclear. Here, we found that microdomains of phosphatidylinositol 4-phosphate (PI(4)P) on Trans-Golgi network (TGN) vesicles were recruited to mitochondria-ER contact sites and could drive mitochondrial division downstream of Drp1. The loss of the small GTPase ADP-ribosylation factor 1 (Arf1) or its effector, phosphatidylinositol 4-kinase IIIβ (PI(4)KIIIβ) in different mammalian cell lines, prevented PI(4)P generation and led to a hyperfused and branched mitochondrial network, marked with extended mitochondrial constriction sites. Thus, recruitment of TGN-PI(4)P-containing vesicles at mitochondria-ER contact sites may trigger final events leading to mitochondrial scission.

Mitochondrial division is initiated at sites where the endoplasmic reticulum (ER) contacts mitochondria, which mark the site of constriction and subsequent recruitment of the large GTPase Dynamin-related protein-1 (Drp1) (*1*). At these sites, Drp1 oligomerization further enhances mitochondrial constriction driven by GTP-hydrolysis (*2*). It has been suggested that the GTPase Dynamin 2 (Dnm2), is required downstream of Drp1-mediated constriction to terminate membrane scission (*3*); however, its precise contribution and the molecular details of late events are currently unclear (*4, 5*). A growing body of evidence supports the role of other factors regulating mitochondrial division including phospholipids, calcium and lysosomes (*6*). Furthermore, a recent study revealed that loss of the small GTPase ADP-ribosylation factor 1 (Arf1) led to alterations in mitochondrial morphology with hyperfusion in *C.elegans* (*7*). GTP-bound Arf1 is recruited primarily to the Golgi apparatus where it is canonically known for its role in the generation of COP1 coated vesicles. GTP specific effector proteins of Arf1 include phosphatidylinositol 4-kinase-III-β (PI(4)KIIIβ), which mediates the phosphorylation of phosphatidylinositol to generate phosphatidylinositol 4-phosphate (PI(4)P) (*8*). This generates lipid microdomains enriched for PI(4)P that are required for membrane remodelling events (*9-12*). Given the primary role for these enzymes in membrane dynamics (*7, 13*), we investigated the mechanisms that underlie the contribution of PI(4)P pools in the regulation of mitochondrial morphology.

Silencing of both Arf1 and PI(4)KIIIβ led to mitochondrial hyperfusion in HeLa cells (Fig. 1A-D). In contrast to Drp1-silenced cells, loss of PI(4)KIIIβ and Arf1 induced mitochondrial elongation and mitochondrial branching, leading to a highly interconnected network and an increase of mitochondrial intersections, called junctions (Fig. 1E). These results were confirmed in two other mammalian cell lines, Cos-7 and U2OS cells (Fig. S1A-K). We further quantified mitochondrial interconnectivity using a photo-activatable GFP probe targeted to the mitochondrial

matrix (OCT-PAGFP) (*14*) (Fig. 1F, G). Mitochondrial hyperfusion induced by PI(4)KIIIβ silencing was rescued upon re-expression of the bovine wild-type (WT)-PI(4)KIIIβ (PI4K-HA) but not with the kinase-dead mutant (PI4K-KD-HA) (*15*) (Fig. 1 H, I and Fig. S1L, M). Treatment of HeLa or Cos-7 cells with the selective PI(4)KIIIβ inhibitor PIK93 also resulted in mitochondrial hyperfusion and branching (Fig. S2). In addition, among the PI(4)K family, only PI(4)KIIβ silencing induced mild mitochondrial hyperfusion in HeLa (Fig. S3A-G), but not in Cos-7 cells (Fig. S3H-N), which may co-incident with a cell-type specific decrease of Drp1 and PI(4)KIIIβ protein levels upon silencing (Fig. S3F). Finally, cells silenced for ceramide transfer protein (CERT), another Arf1-effector, did not lead to mitochondrial hyperfusion (Fig. S4). Thus, both the kinase activity of the specific effector PI(4)KIIIβ, and the GTPase, Arf1, are required to modulate mitochondrial dynamics.

In transmission electron microscopy (TEM), PI(4)KIIIβ- and Arf1-silenced cells displayed exaggerated mitochondrial hyperfusion and branching (Fig. 2A-D and Fig. S5A). We observed an accumulation of unusual mitochondrial hyper-constricted sites in cells lacking either Arf1 or PI(4)KIIIβ (Fig. 2E-G and Fig. S5B, C). These sites were characterized by a long and narrow neck, where the inner membrane was observed running parallel with the constricted outer membrane (Fig. 2A, E, F and Fig. S5B). In addition, the ER was in close apposition along these constricted sites (Fig. 2G), suggesting that mitochondria-ER contacts (MERCs) were maintained. A similar level of mitochondrial hyper-constriction has been reported in cells silenced with Dnm2 (*3*), where it has been suggested that this dynamin may act downstream of Drp1 to drive fission. However, silencing Dnm2 in U2OS and HeLa cells failed to recapitulate the mitochondrial hyperfusion and branching phenotype induced by the loss of PI(4)P pools (Fig. S6), as it has recently been reported (*4, 5*), suggesting that Arf1 and PI(4)KIIIβ may not be required for Dnm2 recruitment.

Loss of Arf1 in yeast results in an accumulation of the fusion GTPase Fzo1 at mitochondria and an alteration in mitochondrial morphology (*7*). However, we found no major changes in the levels of the main pro-fission/fusion regulators after 48 or 72 hours of silencing for Arf1 and PI(4)KIIIβ, respectively, in HeLa (Fig. 2H), Cos-7 (Fig. S5D) and U2OS (Fig. S5E). Although Arf1 silencing for 3 days led to ER morphology aberrations and significant levels of cell death (Fig. S7), we still did not observe significant changes in the main fission/fusion regulator levels (Fig. S7D). Immunofluorescence analysis of endogenous Mfn1 and Mfn2 in PI(4)KIIIβ- and Arf1-silenced HeLa cells also did not reveal any aggregation or mislocalization (Fig. S5F, G). In addition, subcellular distribution analyses of Drp1 revealed no mitochondrial recruitment defects (Fig. 2I-K) and striking Drp1 foci specifically at mitochondrial super-constrictions induced by loss of PI(4)KIIIβ in the human fibroblasts, MCH64 (Fig. 2K). Furthermore, stimulated Drp1-dependent mitochondrial fission induced by mitochondrial-anchored protein ligase (MAPL) (*16*) overexpression (Fig. S8A, B) or by Carbonyl Cyanide Chlorophenylhydrazone (CCCP) treatment (Fig. S8C, D), was significantly reduced in PI(4)KIIIβ- and Arf1-silenced cells. Silencing of the key component involved in stress-induced mitochondrial hyperfusion, SLP-2 (*17*), as well as the pro-fusion factors Mfn1 and Mfn2, also failed to reverse mitochondrial hyperfusion in PI(4)KIIIβ silenced cells (Fig. S9). Finally, compared to Drp1 silencing, which leads to drastic peroxisomal elongation (*18, 19*), loss of Arf1 and PI(4)KIIIβ only induced a subtle peroxisomal elongation in HeLa, but not in Cos-7 cells (Fig. S10). Thus, these data potentially support a specific role for these enzymes in the regulation of mitochondrial fission downstream of Drp1 recruitment.

PI(4)KIIIβ mainly localized to the Golgi apparatus (Fig. S11A), but PI(4)KIIIβ foci were also detected at ER-induced mitochondrial constriction sites (Fig. 3A and Fig. S11B). Similar results were obtained for subcellular localization analysis of Arf1-GFP (Fig. S11C). Their presence

at the MERC compartment was confirmed by subcellular fractionation experiment (Fig. 3B). We then performed live cell imaging to monitor whether Arf1-GFP was recruited to mitochondrial constriction sites before division (Fig. 3C and Movies. S1, S2). Around 71% of mitochondrial division events analysed were marked with Arf1-GFP punctae before fission (Fig. 3D) and 77% of division events showed the recruitment of these punctae at constriction sites after Drp1 recruitment (Fig. 3E, F and Movie. S3). While Arf1-GFP foci were preferentially found on ER-induced mitochondrial constriction sites (Fig. S11D and Movies. S4, S5), Arf1-GFP foci were not localized at mitochondrial tip-ends after division (Fig. 3C, D and Movies. S1, S2), and they did not localize perfectly with ER markers (Fig. S11D). This suggested that Arf1 was primarily recruited to the MERC during division from a ternary compartment. Previous work uncovered a role for lysosomes at sites of mitochondrial division (*20*), so we first explored whether Arf1-GFP foci may reflect these structures. However, while Arf1-GFP foci converged with lysosomes at fission sites, its recruitment was distinct from lysosomes (Fig. 3G, H and Movie. S6). Instead, we found that Arf1-GFP foci were recruited to constriction sites upon Trans-Golgi network (TGN) vesicles (Fig. 3I, J and Movie. S7). Indeed, TGN46-mCherry vesicles were recruited to mitochondrial constriction just before division in 85% of fission events analysed, which was correlated by a colocalization with Arf1-GFP punctae before and during this process in 80% of division events (Fig. 3I, J and Movie. S7).

We confirmed the predominant Golgi localization for PI(4)P (Fig. S12A) using the established probe GFP-PH^{FAPP1} (*21*), but we also observed PI(4)P enriched foci crossing ER-induced mitochondrial constriction sites (Fig. 4A), in an Arf1- and PI(4)KIIIβ-dependent manner (Fig. S12B, C). Loss of Drp1 also significantly decreased mitochondrial GFP-PH^{FAPP1} punctae suggesting that Drp1 activity was required for the recruitment of TGN-derived PI(4)P vesicles

(Fig. S12B, C). Video analysis revealed pools of PI(4)P accumulated and extended towards mitochondria at sites of constriction (Fig. 4B and Movies. S8, S9), in around 73% of division events analysed (Fig. 4B, C). Similar to Arf1-GFP, PI(4)P foci were recruited to MERCs downstream of Drp1 (Fig. 4D, E, Fig. S13 and Movies. S10, S11), and remained on TGN46 vesicles throughout the fission event (Fig. 4F, G and Movie. S12). Moreover, we observed no colocalization with lysosomes that converged at the site of division (Fig. 4H, I and Movie. S13). These results were confirmed using an additional PI(4)P probe, mCherry-P4M, which recognizes PI(4)P pools in multiple endomembranes (*22*) (Fig. S14 and Movies. S14-S16). Finally, consistent with the assembly of the mitochondrial fission machinery and the coordination of PI(4)P accumulation, endogenous TGN46, PI(4)KIIIβ and GFP-PH^{FAPP1} foci colocalized with endogenous Drp1 at ER-induced mitochondrial constrictions (Fig. S15). Thus, Arf1 and PI(4)KIIIβ enable the accumulation of PI(4)P puncta on TGN vesicles driving late steps of mitochondrial division.

Mitochondrial fission is a complex process that requires many factors including the ER, involved in the early steps of organelle constriction (*1, 23*) and the lysosomes, recently identified at division sites (*20*). However, the functional contribution of these organelles to the process of membrane fission remains unclear. We now add a further layer of complexity by identifying a key role for Arf1 and PI(4)KIIIβ on Golgi vesicles in driving late steps of mitochondrial division. These data reveal a 4-way contact between mitochondria, ER, TGN and lysosomal vesicles occurring at >80% of fission sites. It is unclear why so many organelles are required to drive mitochondrial division. In considering the contribution of PI(4)P enriched vesicles (*24*), we envision a potential role in the recruitment of adaptors that drive Arp2/3-dependent actin polymerization at transient and localized microdomains that could allow the dynamic assembly of

force-generating machineries essential for the final steps of mitochondrial division (*25-27*). We now suggest that the intimate contacts between mitochondria and the Golgi apparatus, and PI(4)P, are key modulators of mitochondrial dynamics.

REFERENCES

1. J. R. Friedman *et al.*, ER tubules mark sites of mitochondrial division. *Science* **334**, 358-362 (2011).
2. E. Smirnova, L. Griparic, D. L. Shurland, A. M. van der Bliek, Dynamin-related protein Drp1 is required for mitochondrial division in mammalian cells. *Mol Biol Cell* **12**, 2245-2256 (2001).
3. J. E. Lee, L. M. Westrate, H. Wu, C. Page, G. K. Voeltz, Multiple dynamin family members collaborate to drive mitochondrial division. *Nature* **540**, 139-143 (2016).
4. S. C. Kamerkar, F. Kraus, A. J. Sharpe, T. J. Pucadyil, M. T. Ryan, Dynamin-related protein 1 has membrane constricting and severing abilities sufficient for mitochondrial and peroxisomal fission. *Nat Commun* **9**, 5239 (2018).
5. T. B. Fonseca, A. Sanchez-Guerrero, I. Milosevic, N. Raimundo, Mitochondrial fission requires DRP1 but not dynamins. *Nature* **570**, E34-E42 (2019).
6. L. Tilokani, S. Nagashima, V. Paupe, J. Prudent, Mitochondrial dynamics: overview of molecular mechanisms. *Essays Biochem* **62**, 341-360 (2018).
7. K. B. Ackema *et al.*, The small GTPase Arf1 modulates mitochondrial morphology and function. *EMBO J* **33**, 2659-2675 (2014).
8. A. Godi *et al.*, ARF mediates recruitment of PtdIns-4-OH kinase-beta and stimulates synthesis of PtdIns(4,5)P2 on the Golgi complex. *Nat Cell Biol* **1**, 280-287 (1999).
9. B. Mesmin *et al.*, A four-step cycle driven by PI(4)P hydrolysis directs sterol/PI(4)P exchange by the ER-Golgi tether OSBP. *Cell* **155**, 830-843 (2013).
10. J. Moser von Filseck *et al.*, INTRACELLULAR TRANSPORT. Phosphatidylserine transport by ORP/Osh proteins is driven by phosphatidylinositol 4-phosphate. *Science* **349**, 432-436 (2015).
11. J. Moser von Filseck, S. Vanni, B. Mesmin, B. Antonny, G. Drin, A phosphatidylinositol-4-phosphate powered exchange mechanism to create a lipid gradient between membranes. *Nat Commun* **6**, 6671 (2015).
12. J. Chung *et al.*, INTRACELLULAR TRANSPORT. PI4P/phosphatidylserine countertransport at ORP5- and ORP8-mediated ER-plasma membrane contacts. *Science* **349**, 428-432 (2015).
13. J. H. Pogson *et al.*, The complex I subunit NDUFA10 selectively rescues Drosophila pink1 mutants through a mechanism independent of mitophagy. *PLoS Genet* **10**, e1004815 (2014).
14. G. H. Patterson, J. Lippincott-Schwartz, A photoactivatable GFP for selective photolabeling of proteins and cells. *Science* **297**, 1873-1877 (2002).
15. X. H. Zhao, T. Bondeva, T. Balla, Characterization of recombinant phosphatidylinositol 4-kinase beta reveals auto- and heterophosphorylation of the enzyme. *J Biol Chem* **275**, 14642-14648 (2000).
16. E. Braschi, R. Zunino, H. M. McBride, MAPL is a new mitochondrial SUMO E3 ligase that regulates mitochondrial fission. *EMBO Rep* **10**, 748-754 (2009).
17. D. Tondera *et al.*, SLP-2 is required for stress-induced mitochondrial hyperfusion. *EMBO J* **28**, 1589-1600 (2009).

18. X. Li, S. J. Gould, The dynamin-like GTPase DLP1 is essential for peroxisome division and is recruited to peroxisomes in part by PEX11. *J Biol Chem* **278**, 17012-17020 (2003).
19. A. Koch *et al.*, Dynamin-like protein 1 is involved in peroxisomal fission. *J Biol Chem* **278**, 8597-8605 (2003).
20. Y. C. Wong, D. Ysselstein, D. Krainc, Mitochondria-lysosome contacts regulate mitochondrial fission via RAB7 GTP hydrolysis. *Nature* **554**, 382-386 (2018).
21. S. Dowler *et al.*, Identification of pleckstrin-homology-domain-containing proteins with novel phosphoinositide-binding specificities. *Biochem J* **351**, 19-31 (2000).
22. G. R. Hammond, M. P. Machner, T. Balla, A novel probe for phosphatidylinositol 4-phosphate reveals multiple pools beyond the Golgi. *J Cell Biol* **205**, 113-126 (2014).
23. F. Korobova, V. Ramabhadran, H. N. Higgs, An actin-dependent step in mitochondrial fission mediated by the ER-associated formin INF2. *Science* **339**, 464-467 (2013).
24. R. Dong *et al.*, Endosome-ER Contacts Control Actin Nucleation and Retromer Function through VAP-Dependent Regulation of PI4P. *Cell* **166**, 408-423 (2016).
25. E. Derivery *et al.*, The Arp2/3 activator WASH controls the fission of endosomes through a large multiprotein complex. *Dev Cell* **17**, 712-723 (2009).
26. S. Li *et al.*, Transient assembly of F-actin on the outer mitochondrial membrane contributes to mitochondrial fission. *J Cell Biol* **208**, 109-123 (2015).
27. N. H. Hong, A. Qi, A. M. Weaver, PI(3,5)P2 controls endosomal branched actin dynamics by regulating cortactin-actin interactions. *J Cell Biol* **210**, 753-769 (2015).
28. H. Lochmuller, T. Johns, E. A. Shoubridge, Expression of the E6 and E7 genes of human papillomavirus (HPV16) extends the life span of human myoblasts. *Exp Cell Res* **248**, 186-193 (1999).
29. R. Zunino, A. Schauss, P. Rippstein, M. Andrade-Navarro, H. M. McBride, The SUMO protease SENP5 is required to maintain mitochondrial morphology and function. *J Cell Sci* **120**, 1178-1188 (2007).
30. E. Braschi *et al.*, Vps35 mediates vesicle transport between the mitochondria and peroxisomes. *Curr Biol* **20**, 1310-1315 (2010).
31. R. N. Day, M. W. Davidson, The fluorescent protein palette: tools for cellular imaging. *Chem Soc Rev* **38**, 2887-2921 (2009).
32. D. S. Bindels *et al.*, mScarlet: a bright monomeric red fluorescent protein for cellular imaging. *Nat Methods* **14**, 53-56 (2017).
33. J. Chun, Z. Shapovalova, S. Y. Dejgaard, J. F. Presley, P. Melancon, Characterization of class I and II ADP-ribosylation factors (Arfs) in live cells: GDP-bound class II Arfs associate with the ER-Golgi intermediate compartment independently of GBF1. *Mol Biol Cell* **19**, 3488-3500 (2008).
34. G. R. Hammond, M. P. Machner, T. Balla, A novel probe for phosphatidylinositol 4-phosphate reveals multiple pools beyond the Golgi. *J Cell Biol* **205**, 113-126 (2014).
35. A. Sugiura, S. Mattie, J. Prudent, H. M. McBride, Newly born peroxisomes are a hybrid of mitochondrial and ER-derived pre-peroxisomes. *Nature* **542**, 251-254 (2017).
36. J. Prudent *et al.*, MAPL SUMOylation of Drp1 Stabilizes an ER/Mitochondrial Platform Required for Cell Death. *Mol Cell* **59**, 941-955 (2015).
37. J. Schindelin *et al.*, Fiji: an open-source platform for biological-image analysis. *Nat Methods* **9**, 676-682 (2012).
38. J. E. Lee, L. M. Westrate, H. Wu, C. Page, G. K. Voeltz, Multiple dynamin family members collaborate to drive mitochondrial division. *Nature* **540**, 139-143 (2016).

39. A. S. Moore, Y. C. Wong, C. L. Simpson, E. L. Holzbaur, Dynamic actin cycling through mitochondrial subpopulations locally regulates the fission-fusion balance within mitochondrial networks. *Nat Commun* **7**, 12886 (2016).
40. I. Arganda-Carreras, R. Fernandez-Gonzalez, A. Munoz-Barrutia, C. Ortiz-De-Solorzano, 3D reconstruction of histological sections: Application to mammary gland tissue. *Microsc Res Tech* **73**, 1019-1029 (2010).
41. C. D. Williamson, D. S. Wong, P. Bozidis, A. Zhang, A. M. Colberg-Poley, Isolation of Endoplasmic Reticulum, Mitochondria, and Mitochondria-Associated Membrane and Detergent Resistant Membrane Fractions from Transfected Cells and from Human Cytomegalovirus-Infected Primary Fibroblasts. *Curr Protoc Cell Biol* **68**, 3 27 21-33 (2015).

ACKNOWLEDGMENTS

We thank Sevan Mattie for its contribution to transmission electronic microscopy samples preparation and images acquisition. **Funding:** This work was supported by the Canadian Institutes of Health Research Operating Grants Program (CIHR#68833) to H.M.M., Medical Research Council funding (MC_UU_00015/7 and RG89175), Isaac Newton Trust (RG89529) and Wellcome Trust Institutional Strategic Support Fund (RG89305) to J.P. H.M.M. is a Canada Research Chair. S.N. and L.C.T. are recipients of a Daiichi Sankyo Foundation of Life Science and Ramon Areces postdoctoral fellowships, respectively. L.T. is supported by a MRC-funded graduate student fellowship. V.P was supported by the European Union's Horizon 2020 research and innovation programme (MITODYN-749926). **Authors contributions:** S.N. performed the experiments; L.C.T. and L.T. contributed to quantitative confocal imaging and immunoblots analysis; V.P. carried-out organelle fractionation; H.A. provided technical assistance; J.H.P. contributed intellectually to the initial development of the project; R.Z. contributed to biochemical analysis; H.M.M. and J.P. conceived the study, designed the experiments and wrote the manuscript. **Competing interests:** The authors declare no competing interest. **Data and materials availability:** All data are available in the manuscript or the supplementary materials.

SUPPLEMENTARY MATERIALS

Materials and Methods

Table S1

Figs S1 – S15

References (28 – 41)

Movies S1 – S16

Figure 1

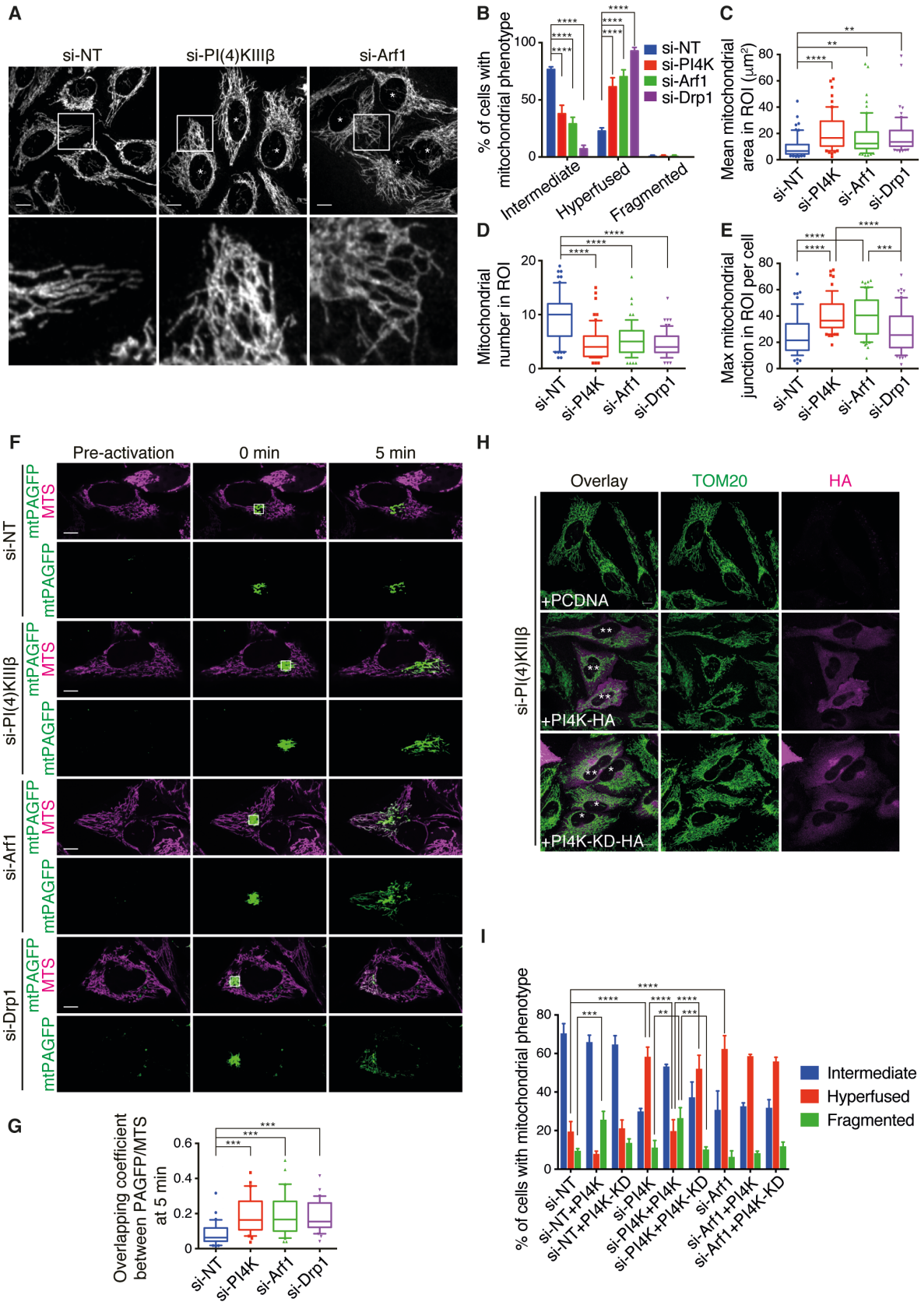
A
si-NT
si-PI(4)KIIIβ
si-Arf1
B
% of cells with mitochondrial phenotype
si-NT
si-PI4K
si-Arf1
si-Drp1
Intermediate
Hyperfused
Fragmented
C
Mean mitochondrial area in ROI (μm²)
si-NT
si-PI4K
si-Arf1
si-Drp1
D
Mitochondrial number in ROI
E
Max mitochondrial junction in ROI per cell
F
Pre-activation
0 min
5 min
mtPAGFP
MTS
G
Overlapping coefficient between PAGFP/MTS at 5 min
H
Overlay
TOM20
HA
+PCDNA
+PI4K-HA
+PI4K-KD-HA
I
% of cells with mitochondrial phenotype
si-NT
si-NT+PI4K
si-NT+PI4K-KD
si-PI4K
si-PI4K+PI4K
si-PI4K+PI4K-KD
si-Arf1
si-Arf1+PI4K
si-Arf1+PI4K-KD

Fig. 1. Arf1 and PI(4)KIIIβ silencing leads to mitochondrial hyperfusion and branching. (A) Representative confocal images of mitochondrial morphology in HeLa cells treated with indicated siRNAs. Mitochondria were labelled using an anti-TOM20 antibody. * indicates cells with elongated/branched mitochondria. **(B)** Quantification of mitochondrial morphology from (A). **(C-E)** Mitochondrial morphology was quantified for **(C)** mean mitochondrial area per mitochondrion, **(D)** mitochondrial number and **(E)** mitochondrial branching measured by maximum mitochondrial junction number, per region of interest (ROI). **(F)** Live cell imaging of HeLa cells treated with indicated siRNAs, overexpressing the OCT-photo-activatable GFP (mt-PAGFP) probe and the mitochondrial marker MTS-Scarlet (MTS). **(G)** Quantification of the OCT-PAGFP probe diffusion over 5 min period from (F) using the overlapping Mander's coefficient. **(H)** Representative confocal images of mitochondrial morphology in HeLa cells silenced with PI(4)KIIIβ siRNA, transiently overexpressing empty vector (vehicle), WT-PI(4)KIIIβ-HA (PI4K-HA) and kinase-dead mutant PI(4)KIIIβ-HA (PI4K-KD-HA). * and ** indicate HA-positive transfected cells with * elongated/branched mitochondria and ** intermediate mitochondria. **(I)** Quantification of mitochondrial morphology from (H) and Fig. S1L. All scale bars: 10 μm. All values: mean ± SD; at least three independent experiments; (B, I): two-way ANOVA, Tukey's multiple comparisons test; (C-E, G): ordinary one-way ANOVA, Tukey's multiple comparisons test. See also Table S1.

Figure 2

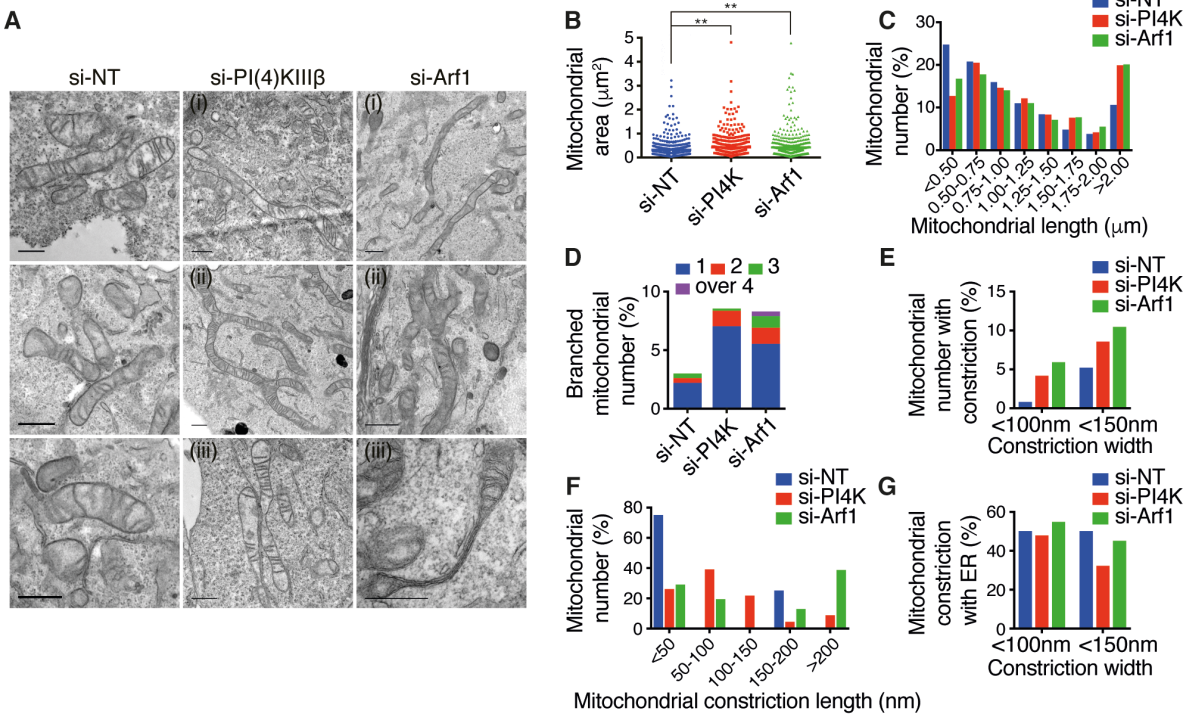
A
si-NT
si-PI(4)KIIIβ
si-Arf1
(i)
(ii)
(iii)
B
Mitochondrial area (μm²)
si-NT
si-PI4K
si-Arf1
**
**
C
Mitochondrial number (%)
si-NT
si-PI4K
si-Arf1
<0.50
0.50-0.75
0.75-1.00
1.00-1.25
1.25-1.50
1.50-1.75
1.75-2.00
>2.00
Mitochondrial length (μm)
D
Branched mitochondrial number (%)
1
2
3
over 4
si-NT
si-PI4K
si-Arf1
E
Mitochondrial number with constriction (%)
si-NT
si-PI4K
si-Arf1
<100nm
<150nm
Constriction width
F
Mitochondrial number (%)
si-NT
si-PI4K
si-Arf1
<50
50-100
100-150
150-200
>200
Mitochondrial constriction length (nm)
G
Mitochondrial constriction with ER (%)
si-NT
si-PI4K
si-Arf1
<100nm
<150nm
Constriction width

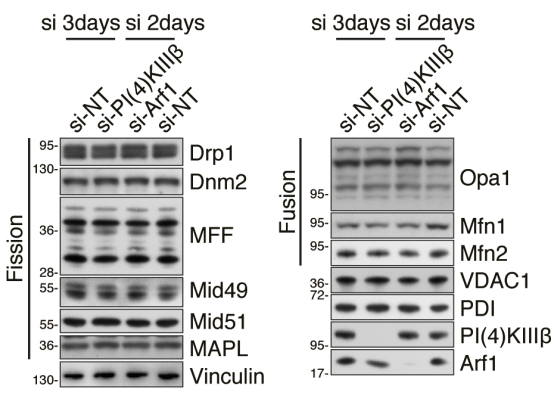
H
si 3days
si 2days
si-NT
si-PI(4)KIIIβ
si-Arf1
si-NT
Fission
Drp1
Dnm2
MFF
Mid49
Mid51
MAPL
Vinculin
Fusion
Opa1
Mfn1
Mfn2
VDAC1
PDI
PI(4)KIIIβ
Arf1

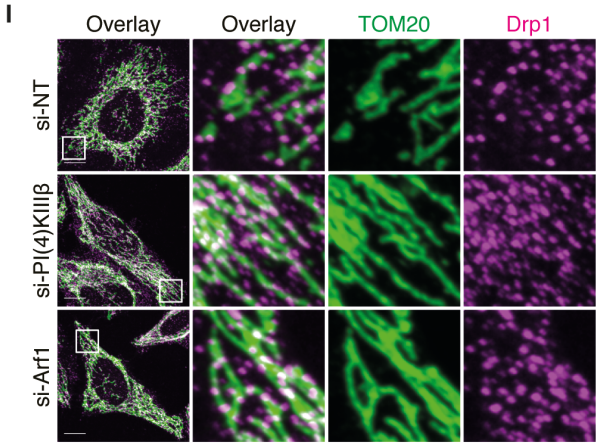
I
Overlay
Overlay
TOM20
Drp1
si-NT
si-PI(4)KIIIβ
si-Arf1

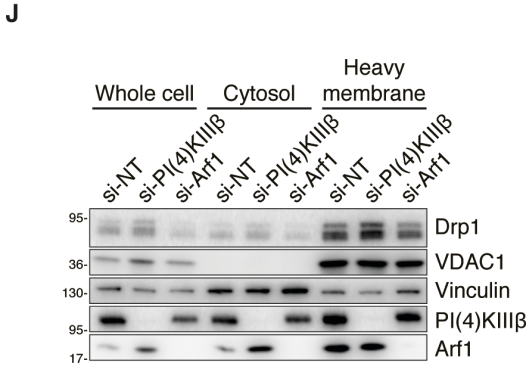
J
Whole cell
Cytosol
Heavy membrane
si-NT
si-PI(4)KIIIβ
si-Arf1
Drp1
VDAC1
Vinculin
PI(4)KIIIβ
Arf1

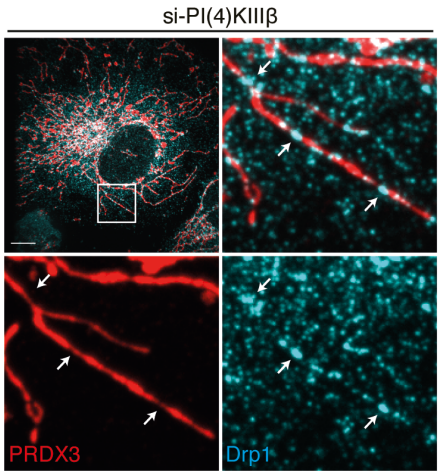
K
si-PI(4)KIIIβ
PRDX3
Drp1

Fig. 2. Loss of Arf1 and PI(4)KIIIβ induces mitochondrial super-constriction sites and does not alter fusion/fission machinery. (A) Representative transmission electron microscopy (TEM) images of HeLa cells treated with indicated siRNAs, showing (i) hyperfused mitochondria, (ii) branched mitochondria, and (iii) mitochondrial super-constriction sites with endoplasmic reticulum (ER) contacts. Scale bars: 500 nm. **(B-G)** Quantification of TEM images from (A) showing **(B)** mitochondrial area, **(C)** distribution of mitochondrial length, **(D)** percentage of branched mitochondria with indicated branch count, **(E)** percentage of mitochondria harboring mitochondrial super-constrictions, **(F)** distribution of mitochondrial super-constrictions length (width is less than 100 nm), and **(G)** percentage of mitochondrial super-constriction with ER contacts. **(H)** Levels of proteins relevant to mitochondrial fission (left panel) and fusion (right panel) from HeLa cells treated with indicated siRNAs. **(I)** Representative confocal images of mitochondrial morphology and Drp1 localization in HeLa cells treated with indicated siRNAs. Scale bars: 10 μm. **(J)** Subcellular fractionation analysis of Drp1 distribution in HeLa cells treated with indicated siRNAs. Total cell lysates (Whole cell) were fractionated into crude mitochondrial (heavy membrane) and cytosolic (cytosol) fractions. **(K)** Representative confocal images of Drp1 accumulating at mitochondrial super-constriction sites (white arrows) in human fibroblasts silenced for PI(4)KIIIβ. Scale bar: 10 μm. For (B): ordinary one-way ANOVA, Tukey's multiple comparisons test; 2 independent experiments.

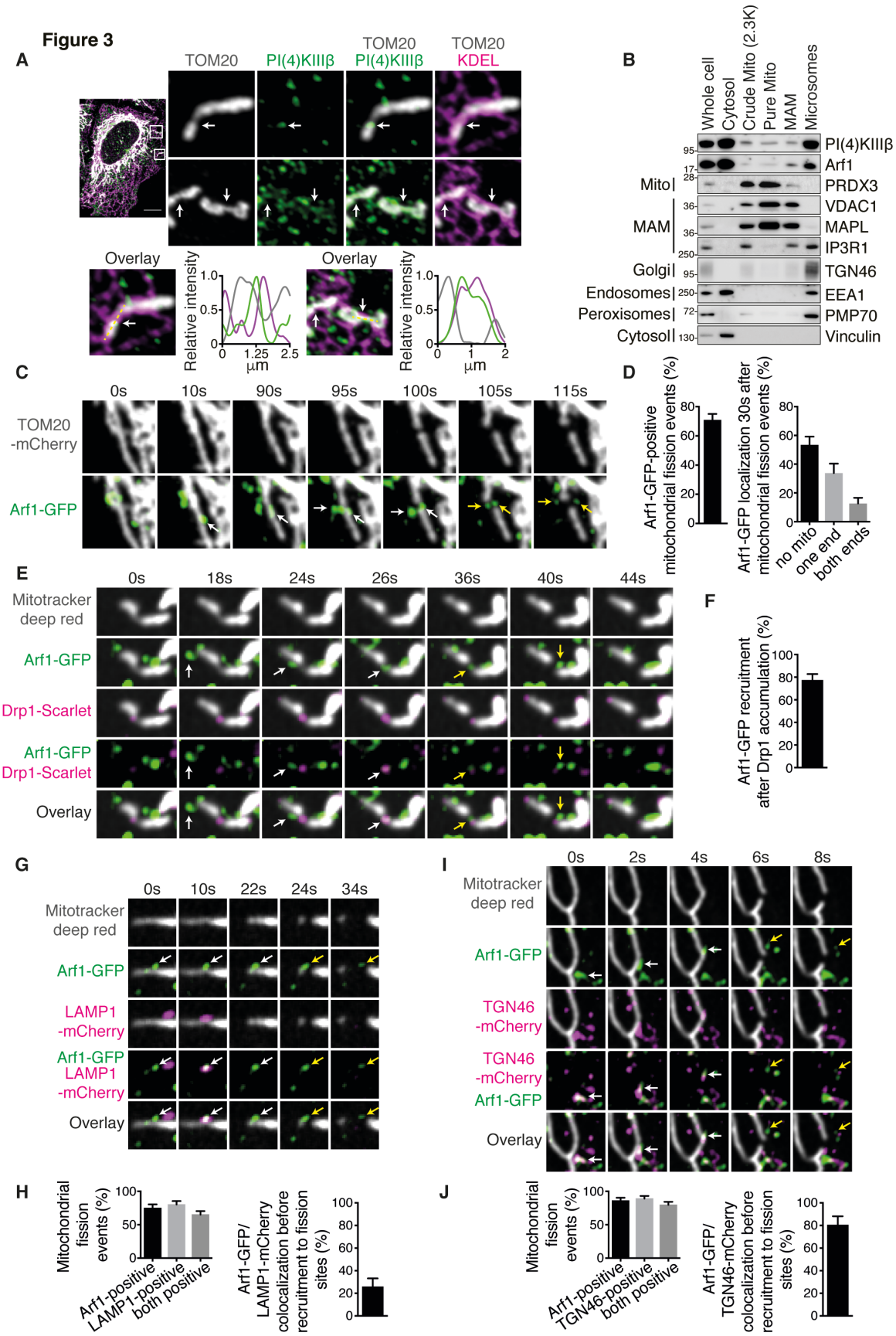
Figure 3
A
TOM20
PI(4)KIIIβ
TOM20
PI(4)KIIIβ
TOM20
KDEL
Overlay
Relative intensity
μm
Overlay
Relative intensity
μm
B
Whole cell
Cytosol
Crude Mito (2.3K)
Pure Mito
MAM
Microsomes
PI(4)KIIIβ
Arf1
PRDX3
VDAC1
MAPL
IP3R1
TGN46
EEA1
PMP70
Vinculin
Mito
MAM
Golgi
Endosomes
Peroxisomes
Cytosol
C
0s
10s
90s
95s
100s
105s
115s
TOM20
-mCherry
Arf1-GFP
D
Arf1-GFP-positive mitochondrial fission events (%)
Arf1-GFP localization 30s after mitochondrial fission events (%)
no mito
one end
both ends
E
0s
18s
24s
26s
36s
40s
44s
Mitotracker deep red
Arf1-GFP
Drp1-Scarlet
Arf1-GFP
Drp1-Scarlet
Overlay
F
Arf1-GFP recruitment after Drp1 accumulation (%)
G
0s
10s
22s
24s
34s
Mitotracker deep red
Arf1-GFP
LAMP1
-mCherry
Arf1-GFP
LAMP1
-mCherry
Overlay
I
0s
2s
4s
6s
8s
Mitotracker deep red
Arf1-GFP
TGN46
-mCherry
TGN46
-mCherry
Arf1-GFP
Overlay
H
Mitochondrial fission events (%)
Arf1-positive
LAMP1-positive
both positive
Arf1-GFP/
LAMP1-mCherry
colocalization before
recruitment to fission
sites (%)
J
Mitochondrial fission events (%)
Arf1-positive
TGN46-positive
both positive
Arf1-GFP/
TGN46-mCherry
colocalization before
recruitment to fission
sites (%)

Fig. 3. PI(4)KIIIβ and Arf1 localized on TGN vesicles are recruited to mitochondrial constrictions and ER contacts prior division. (A) Representative images of PI(4)KIIIβ punctae localization at mitochondrial constriction sites and ER contacts in HeLa cells (white arrows). Line-scan analysis of relative fluorescence intensity from the dashed line are shown. **(B)** PI(4)KIIIβ and Arf1 localization analysis by subcellular fractionation from HeLa cells. Total cell lysates (Whole cell) were fractionated into cytosolic, heavy membrane (crude mito), purified mitochondrial (pure mito), mitochondria-associated membranes (MAM) and microsomal (microsomes) fractions. **(C)** Live cell imaging of HeLa cells transiently expressing Arf1-GFP and TOM20-mCherry. **(D)** Quantification of mitochondrial fission events marked by Arf1-GFP prior division (left panel) and Arf1-GFP dynamics on mitochondria after division (right panel). **(E)** Live cell imaging of HeLa cells transiently expressing Arf1-GFP, Drp1-Scarlet with mitochondria labelled using Mitotracker deep red. **(F)** Quantification of mitochondrial fission events marked by Arf1-GFP downstream of Drp1-Scarlet recruitment. **(G)** Live cell imaging of HeLa cells transiently expressing Arf1-GFP, LAMP1-mCherry with mitochondria labelled using Mitotracker deep red. **(H)** Quantification of mitochondrial fission events marked by Arf1-GFP, LAMP1-mCherry or double Arf1-GFP/LAMP1-mCherry prior division (left panel) and Arf1-GFP/LAMP1-mCherry dynamics before recruitment to division sites (right panel). **(I)** Live cell imaging of HeLa cells transiently expressing Arf1-GFP, TGN46-mCherry with mitochondria labelled using Mitotracker deep red. **(J)** Quantification of mitochondrial fission events marked by Arf1-GFP, TGN46-mCherry or double Arf1-GFP/TGN46-mCherry prior division (left panel) and Arf1-GFP/TGN46-mCherry dynamics before recruitment to division sites (right panel). (C, E, G and I), white and yellow arrows indicate Arf1-GFP puncta prior and after a fission event, respectively. All scale bars: 10 μm. All values: mean ± SEM; at least three independent experiments.

Figure 4

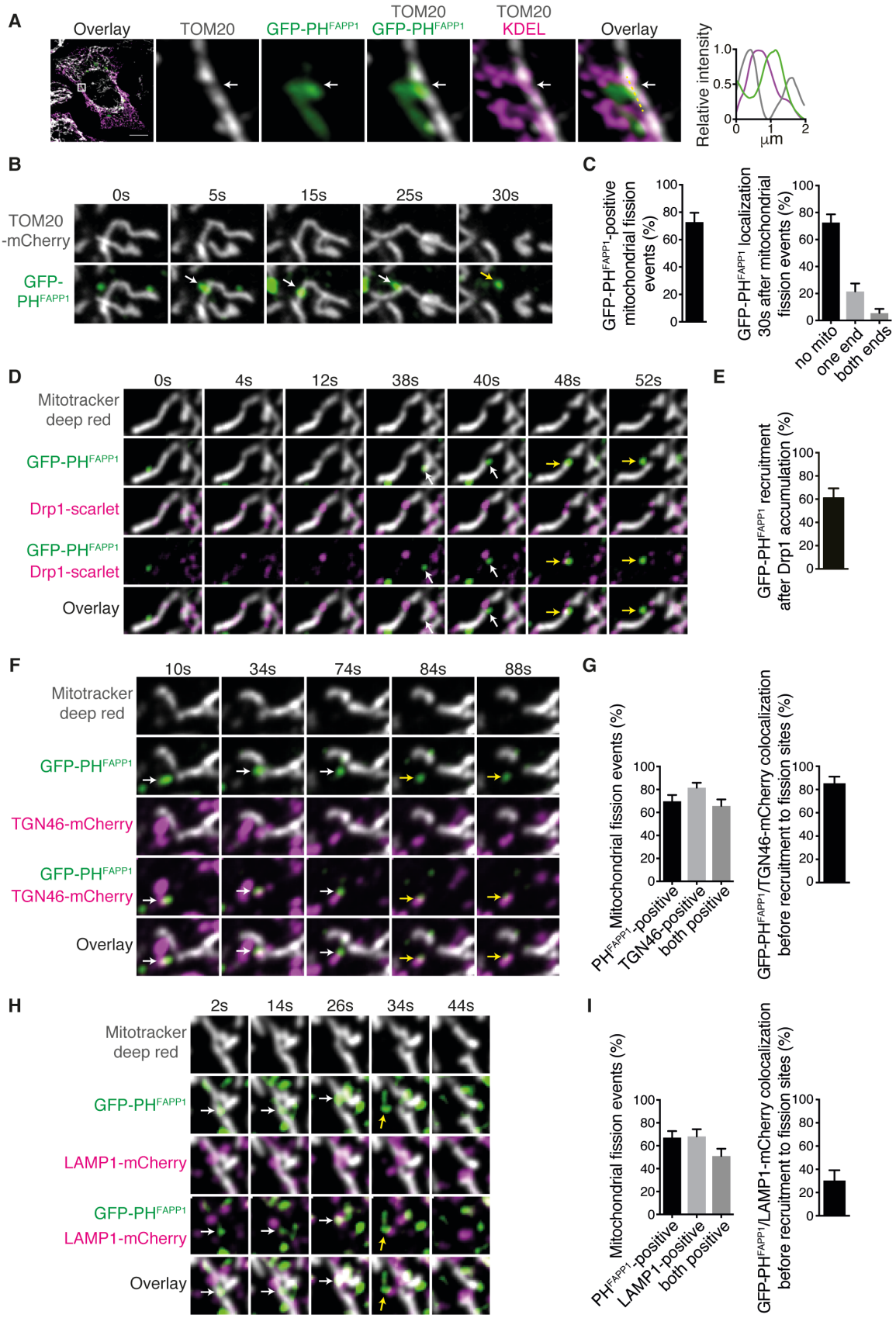
A
Overlay
TOM20
GFP-PH^FAPP1
TOM20 GFP-PH^FAPP1
TOM20 KDEL
Overlay
Relative intensity
1.0
0.5
0
0
1
2
μm
B
0s
5s
15s
25s
30s
TOM20 -mCherry
GFP-PH^FAPP1
C
GFP-PH^FAPP1-positive mitochondrial fission events (%)
GFP-PH^FAPP1 localization 30s after mitochondrial fission events (%)
no mito
one end
both ends
D
0s
4s
12s
38s
40s
48s
52s
Mitotracker deep red
GFP-PH^FAPP1
Drp1-scarlet
GFP-PH^FAPP1 Drp1-scarlet
Overlay
E
GFP-PH^FAPP1 recruitment after Drp1 accumulation (%)
F
10s
34s
74s
84s
88s
Mitotracker deep red
GFP-PH^FAPP1
TGN46-mCherry
GFP-PH^FAPP1 TGN46-mCherry
Overlay
G
Mitochondrial fission events (%)
PH^FAPP1-positive
TGN46-positive
both positive
GFP-PH^FAPP1/TGN46-mCherry colocalization before recruitment to fission sites (%)
H
2s
14s
26s
34s
44s
Mitotracker deep red
GFP-PH^FAPP1
LAMP1-mCherry
GFP-PH^FAPP1 LAMP1-mCherry
Overlay
I
Mitochondrial fission events (%)
PH^FAPP1-positive
LAMP1-positive
both positive
GFP-PH^FAPP1/LAMP1-mCherry colocalization before recruitment to fission sites (%)

Fig. 4. Arf1- and PI(4)KIIIβ-dependent PI(4)P formation on TGN vesicles at mitochondrial constriction and ER contacts drive mitochondrial fission. (A) Representative confocal images of HeLa cells transfected with GFP-PH^{FAPP1} showing GFP-PH^{FAPP1} at mitochondrial constriction sites and ER contacts localization (white arrows). Line-scan analysis of relative fluorescence intensity from the dashed line are shown. **(B)** Live cell imaging of HeLa cells transiently expressing GFP-PH^{FAPP1} and TOM20-mCherry. **(C)** Quantification of mitochondrial fission events marked by GFP-PH^{FAPP1} prior division (left panel) and 30 sec after division (right panel). **(D)** Live cell imaging of HeLa cells transiently expressing GFP-PH^{FAPP1}, Drp1-Scarlet with mitochondria labelled using Mitotracker deep red. **(E)** Quantification of mitochondrial fission events marked by GFP-PH^{FAPP1} downstream of mitochondrial Drp1-Scarlet recruitment. **(F)** Live cell imaging of HeLa cells transiently expressing GFP-PH^{FAPP1}, TGN46-mCherry with mitochondria labelled using Mitotracker deep red. **(G)** Quantification of mitochondrial fission events marked by GFP-PH^{FAPP1}, TGN46-mCherry or double GFP-PH^{FAPP1}/TGN46-mCherry prior division (left panel) and GFP-PH^{FAPP1}/TGN46-mCherry dynamics before recruitment to mitochondrial division sites (right panel). **(H)** Live cell imaging of HeLa cells transiently expressing GFP-PH^{FAPP1}, LAMP1-mCherry with mitochondria labelled using Mitotracker deep red. **(I)** Quantification of mitochondrial fission events marked by GFP-PH^{FAPP1}, LAMP1-mCherry or double GFP-PH^{FAPP1}/LAMP1-mCherry prior division (left panel) and GFP-PH^{FAPP1}/LAMP1-mCherry dynamics before recruitment to mitochondrial division sites (right panel). For (B, D, F and H), white and yellow arrows indicate GFP-PH^{FAPP1} puncta prior and after a fission event, respectively. All scale bars: 10 μm. All values: mean ± SEM; at least three independent experiments.

Science
AAAS

Supplementary Materials for

Golgi derived PI(4)P-containing vesicle drives late steps of mitochondrial division

Shun Nagashima, Luis-Carlos Tabara[†], Lisa Tilokani[†], Vincent Paupe, Hanish Anand, Joe H. Pogson, Rodolfo Zunino, Heidi M. McBride[*] and Julien Prudent[*]

[†] These authors contributed equally to this work.
[*] Corresponding author. E-mail: heidi.mcbride@mcgill.ca; julien.prudent@mrc-mbu.cam.ac.uk

This PDF file includes:

Materials and Methods
Figs. S1 to S15

Other Supplementary Materials for this manuscript include the following:

Table S1
Movies S1 to S16

Materials and Methods

Cell culture and transfections

HeLa, Cos-7 and U20S cells were obtained from American Type Culture Collection (ATCC) and the human fibroblast line MCH64, was obtained from Montreal Children's Hospital cell repository and immortalized, as previously described (*28*). HeLa and Cos-7 cells were cultured in Dulbecco's Modified Eagles Medium (DMEM) and U2OS cells in McCoy's medium, high glucose supplemented with 10% fetal bovine serum (FBS), 2 mM L-glutamine, non-essential amino acids and 100 units/mL penicillin/streptomycin (all from GIBCO) at 37°C with 5% CO_2. Cells were transfected for 24 hours (hr) using FuGene HD (Roche) or Lipofectamine 3000 (Invitrogen) reagents following manufacturers' instructions. For small interference (si) RNA experiments, cells were transfected using Lipofectamine RNAimax (Invitrogen) with 20-30 nM siRNA for 3 days, following manufacturer's instructions. Arf1 silencing was performed for 2 days, except for cell death and ER morphology analysis (Fig. S7) where Arf1 was silenced for 3 days. Cells were tested for mycoplasma contamination using the Lookout Mycoplasma PCR detection kit (Sigma).

Plasmids and reagents

pOCT-PA-GFP and MAPL-FLAG were previously described (*29, 30*). EGFP-hFAPP1(PH) (GFP-PH^{FAPP1}) plasmid was obtained as gift from Marino Zerial (Max Planck Institute of Molecular Cell Biology and Genetics, Dresden, Germany). PI(4)KIIIβ-HA-WT and PI(4)KIIIβ-HA-KD plasmids were obtained as gift from Tamas Balla (Eunice Kennedy Shriver National Institute of Child Health and Human Development, National Institutes of Health, Bethesda, Maryland, USA). DsRed2-ER-5, mCherry-TOMM20-N-10, mEmerald-TOMM20-N-10, mCherry-TGNP-N-10, and mCherry-Lysosomes-20 were gifts from Michael Davidson (Addgene #558361, #55146, #54282, #55145, #55073) (*31*), pmScarlet_Giantin_C1, pmScarlet_C1 and pMTS_mScarlet_N1 were gifts from Dorus Gadella (Addgene #85048, #85042, #850572) (*32*), Arf1-GFP was a gift from Paul Melancon (Addgene #395543) (*33*), mCherry-P4M-SidM and GFP-P4M-SidMx2 were gifts from Tamas Balla (Addgene #514714, #514724) (*34*), mCherry-Drp1 was a gift from Gia Voeltz (Addgene #49152) (*1*). To clone Drp1-Scarlet_C1: Drp1 was digested from mCherry-Drp1 vector and inserted into pmScarlet_C1 using XhoI-BamHI restriction sites. PIK93 and CCCP were obtained from Cayman Chemicals and Sigma-Aldrich, respectively. MitoTracker™ Deep Red FM was obtained from ThermoFisher Scientific.

siRNA Oligonucleotides

Non targeting siRNA (ON-TARGETplus SMARTpool, D-0001810-10-20), siRNA targeting Arf1 (ON-TARGETplus SMARTpool, L-011580-00-0005), COL4A3BP/CERT (ONTARGETplus SMARTpool, L-012101-00-0005), Drp1 (ON-TARGETplus SMARTpool, L-012092-00-0005), Dnm2 (ON-TARGETplus individual siRNA, J-004007-00-0005), Mfn1 (ON-TARGETplus SMARTpool, L-010670-01-0005), Mfn2 (ON-TARGETplus SMARTpool, L-012961-00-0005), PI(4)KIIα (ON-TARGETplus SMARTpool, L-006770-00-0005), PI(4)KIIβ (ON-TARGETplus SMARTpool, L-006769-00-0005), PI(4)KIIIα (ON-TARGETplus SMARTpool, L-006776-00-0005), PI(4)KIIIβ (ON-TARGETplus SMARTpool, L-006777-00-0005), STOML2/SLP2 (ON-TARGETplus SMARTpool, L-020518-01-0005), were purchased from Dharmacon. For rescue experiments, three individual siRNAs targeting PI(4)KIIIβ were used in combination (On-Target individual oligos, D-0066777-03/09/21, Dharmacon).

Antibodies

Rabbit polyclonal anti-TOM20 (sc-114515), mouse monoclonal anti-αTubulin (sc-23948), anti-Arf1 (sc-53168), anti-TOM20 (sc-17764), anti-HSP60 (sc-136291) and anti-PI(4)KIIα (sc-390026) were purchased from Santa Cruz Biotechnology. Rabbit polyclonal anti-Arf1 (SAB2100143), anti-MAPL (HPA017681), mouse monoclonal anti-β-Actin (A2228), anti-FLAG (F1804), anti-Vinculin (V4505), anti-PMP70 (SAB4200181), anti-TGN46 (SAB4200355) and rat monoclonal anti-HA (clone 3F10, 11867423001) were purchased from Sigma-Aldrich. Mouse monoclonal anti-PI(4)KIIIβ (611816) and anti-TOM20 (612278) were purchased from BD Biosciences. Rat anti-KDEL (ab50601), rabbit polyclonal anti-Dynamin 2 (ab3457), anti-CERT (ab72536), rabbit monoclonal anti-KDEL (ab176333), mouse monoclonal anti-ATP5A (ab14748), anti-Grp75 (ab2799), and anti-VDAC1 (ab14734) were purchased from Abcam. Mouse monoclonal anti-Drp1 (611113), anti-EEA1 (610456) and anti-OPA1 (612607) were obtained from BD Transduction. Rabbit polyclonal anti-PARP (9542), anti-IP3R1 (8568), anti-Mfn1 (14739), anti-Mfn2 (11925) and anti-PDI (3501) were obtained from Cell Signaling Technology. Rabbit polyclonal anti-MFF (17090-1-AP), anti-Mid49 (16413-1-AP), anti-Mid51 (20164-1-AP), anti-PI(4)KIIIα (12411-1-AP), anti-PEX14 (10594-1-AP), anti-PRDX3 (55087-1-AP), and mouse monoclonal anti-STOML2/SLP2 (60052-1-Ig) were purchased from Proteintech. Rabbit polyclonal anti-Catalase (219010) was purchased from Merck Millipore. Horseradish peroxidase-conjugated anti-rabbit IgG and anti-mouse IgG were purchased from GE Healthcare. For immunofluorescence, donkey anti-mouse, goat anti-mouse IgG1, goat anti-mouse IgG2a, goat anti-rabbit and goat anti-rat, Alexa Fluor 488, 565, 594 or 647 were used as secondary antibodies (Invitrogen).

Transmission Electron Microscopy

Sample preparation was performed as previously described (*35*). Briefly, HeLa cells silenced with si-NT, si-PI(4)KIIIβ or si-Arf1, were fixed with 2.5% gluteraldehyde in 0.1 M cacodylate buffer (pH 7.4) overnight at 4°C. Cells were washed in 0.1 M cacodylate buffer and fixed with 1% osmium tetroxide for 60 minutes (min) at 4°C, then washed with water before staining with saturated aqueous uranyl acetate for 45 min. Cells were dehydrated with a series of increasing ethanol concentrations, followed by acetone before embedding in Spurr epoxy resin. 100 nm thin sections were mounted on 200-mesh copper grids and stained with Reynold's lead. Sections were imaged at 120kV using a FEI Tecnai 12 TEM outfitted with AMT XR80C CCD Camera System, housed in the Facility for Electron Microscopy Research (FEMR) at McGill University, Montreal, Canada. For quantification analysis, mitochondrial length, area and branch of each individual mitochondrion per cell were manually measured using Fiji software. Mitochondrial constriction sites are defined and quantified as mitochondrial width less than 100 nm and 150 nm. Data are shown as 10 to 90% boxplots with the 25th, 50th, and 75th percentiles as the lower, middle, and upper boundaries of the box, respectively, from two independent experiments.

Immunofluorescence

Immunofluorescence were performed as previously described (*36*). Briefly, cells were fixed in 5% paraformaldehyde (PFA) in PBS at 37°C for 15 min, then washed 3 times with PBS, followed by quenching with 50 mM ammonium chloride in PBS. After 3 washes in PBS, cells were permeabilized in 0.1% Triton X-100 in PBS for 10 min, followed by 3 washes in PBS. Cells were then blocked with 10% FBS in PBS, followed by incubation with primary antibodies in 5%

FBS in PBS, for 2 hr at room temperature (RT). After 3 washes with 5% FBS in PBS, cells were incubated with appropriate secondary antibodies (1:1000) for 1 hr at RT. After 3 washes in PBS, coverslips were mounted onto slides using Dako fluorescence mounting medium (Dako).

Confocal Imaging

Stained or live cells were imaged using a 60X or a 100X objective lenses (NA1.4) on a Nikon Eclipse TiE inverted microscope with appropriate lasers using an Andor Dragonfly 500 confocal spinning disk system, equipped with a Zyla 4.2 PLUS sCMOS camera (fixed cells and live cell) or a iXon Ultra 888 EMCCD camera (live cell) (Andor), coupled with Fusion software (Andor). Photo-activation of the region of interest (ROI) (25 μm^2) was performed using a FRAPPA module (Andor).

For mitochondrial morphology analysis, 7 stacks of 0.2 μm each were acquired using the 100X objective. Images were then compiled by "max projection" and mitochondrial morphology was analysed and presented as intermediate, elongated or fragmented. For rescue experiments, images were acquired using a 63X/1.4 plan apochromat objective and with the 488 nm and 561 nm laser lines of a Carl Zeiss LSM880 confocal laser-scanning system on an Axio Observer Z1 microscope (Carl Zeiss), coupled with ZEN software (Carl Zeiss). We classified mitochondria as "fragmented" when the majority of the mitochondria of the cell were short and spherical, "hyperfused" when the majority of the mitochondria of the cell presented highly elongated mitochondria with less than 10 free ends, and "intermediate" when the majority of the mitochondria of the cell were tubular, neither connected or spherical. At least 30 cells per condition were analysed; 3 independent experiments, using Fiji software (*37*).

For mitochondrial area and number analysis, quantification was performed as described previously (*38*). 225 μm^2 of ROI was selected from max projection images and followed by manual thresholding. Mitochondrial area and number in ROI were obtained using the "Analyze particles" plugin in Fiji with a minimum area of 0.1 μm^2. At least 20 cells per condition were analysed; 3 independent experiments.

For mitochondrial junction analysis, quantification was performed as described previously (*39*). Max projection images were processed twice with the "smooth" function in Fiji. The selected mitochondrial ROI (225 μm^2 ROI) was manually thresholded and then skeletonized using "Make Binary" and "Skeletonize" functions in Fiji. Maximum mitochondrial junctions in ROI was obtained using "Analyze Skeleton (2D/3D)" plugin in Fiji (*40*). At least 20 cells per condition were analysed; 3 independent experiments.

For peroxisomal area, number and circularity analysis, max projection images were processed once with the "smooth" function in Fiji. 225 μm^2 of ROI was selected from max projection images and followed by manual thresholding. Peroxisomal area, number and circularity in ROI were obtained using the "Analyze particles" plugin in Fiji with a minimum area of 0.1 μm^2. At least 20 cells per condition were analysed; 3 independent experiments.

For live cell imaging analysis, time-lapse videos were acquired over the course of 3 or 5 min with each channel captured every 2 or 5 sec. Arf1-GFP, GFP-PH^{FAPP1} and mCherry-P4M foci crossing mitochondria 0-30 sec before mitochondrial division were counted as Arf1-GFP-, GFP-PH^{FAPP1}- and mCherry-P4M-positive mitochondrial fission events, respectively.

To quantify GFP-PH^{FAPP1} foci crossing mitochondria, confocal images of cells overexpressing GFP-PH^{FAPP1} and mitochondria, labelled with anti-TOM20 antibody, were manually analysed. GFP-PH^{FAPP1} foci were considered at mitochondria when they were partially

or totally colocalizing with mitochondria. At least 30 cells per condition were analysed; 3 independent experiments.

The representative images were processed once with the "smooth" function in Fiji.

For quantification, number of cells are presented from 3 independent experiments, otherwise specified. Fig. 1B: n = 158, 153, 155, 153 cells for si-NT, si-PI(4)KIIIβ, si-Arf1 and si-Drp1, respectively. Fig. 1C-E: n = 60 cells. Fig. 1G: n = 60 cells. For (C-E) and (G) data are shown as 10%-90% boxplots with the 25th, 50th, and 75th percentiles as the lower, middle, and upper boundaries of the box, respectively. Values outside this range are shown as dots. Fig. 1I: n= 206, 185, 179 for si-NT + vehicle, + PI(4)KIIIβ-HA, + PI(4)KIIIβ-KD-HA, respectively; n= 176, 176, 155 cells for si-PI(4)KIIIβ + vehicle, + PI(4)KIIIβ-HA, + PI(4)KIIIβ-KD-HA, respectively; n= 172, 143, 150 cells for si-Arf1 + vehicle, + PI(4)KIIIβ-HA, + PI(4)KIIIβ-KD-HA, respectively. Fig. 2: For (B-E), n= 501, 527, 507 mitochondria for si-NT, si-PI(4)KIIIβ and si-Arf1, respectively, from 2 independent experiments. For (F) and (G), n= 4, 23, 31 mitochondrial constriction less than 100 nm, n= 32, 59, 71 mitochondrial constriction less than 150 nm for si-NT, si-PI(4)KIIIβ and si-Arf1, respectively, from 2 independent experiments. Fig. 3D: n= 21 cells, 123 events (left panel) and n= 21 cells, 86 events (right panel). Fig. 3F: n= 15 cells, 44 events. Fig. 3H: n= 15 cells, 79 events (left panel) and n= 15 cells, 51 events (right panel). Fig. 3J: n= 15 cells, 60 events (left panel) and n= 15 cells, 47 events (right panel). Fig. 4C: n= 14 cells, 63 events (left panel) and n= 14 cells, 41 events (right panel). Fig. 4E: n= 14 cells, 40 events. Fig. 4G: n= 15 cells, 75 events (left panel) and n= 15 cells, 46 events (right panel). Fig. 4I: n= 15 cells, 75 events (left panel) and n= 14 cells, 40 events (right panel). Fig. S1B: n = 153, 153, 153, 163 cells for si-NT, si-PI(4)KIIIβ, si-Arf1 and si-Drp1, respectively. Fig. S1C-E: n = 60 cells. Fig. S1G: n = 154, 156, 161, 150 cells for si-NT, si-PI(4)KIIIβ, si-Arf1 and si-Drp1, respectively. Fig. S1H-J: n = 60 cells. Fig. S2B: n = 157, 158, 163 cells for DMSO, 0.5 μM PIK93 and 1 μM PIK93, respectively. Fig. S2C-E: n = 60 cells. Fig. S2G: n = 155, 159, 156 cells for DMSO, 0.5 μM PIK93 and 1 μM PIK93, respectively. Fig. S2H-J: n = 60 cells. Fig. S3B: n = 163, 153, 157, 165, 164, 161 cells for si-NT, si-PI(4)KIIα, si-PI(4)KIIβ, si-PI(4)KIIIα, si-PI(4)KIIIβ and si-Drp1, respectively. Fig. S3C-E: n = 60 cells. Fig. S3I: n = 152, 155, 154, 155 cells for si-NT, si-PI(4)KIIβ, si-PI(4)KIIIβ and si-Drp1, respectively. Fig. S3J-L: n = 60 cells. Fig. S4B: n = 161, 157, 132 cells for si-NT, si-Arf1 and si-CERT, respectively. Fig. S4D: n = 152, 138, 152 cells for si-NT, si-Arf1 and si-CERT, respectively. Fig. S6B: n = 165, 159, 159, 152 cells for si-NT, si-PI(4)KIIIβ, si-Dnm2 and si-Drp1, respectively. Fig. S6D: n = 167, 176, 164, 167 cells for si-NT, si-PI(4)KIIIβ, si-Dnm2 and si-Drp1, respectively. Fig. S7C: n = 109, 97, 94 cells for si-NT, si-PI(4)KIIIβ, and si-Arf1, respectively, from 2 independent experiments. Fig. S8B: n= 110 cells for si-NT + GFP, n= 127 cells for si-NT + MAPL-FLAG, n= 104 cells for si-PI(4)KIIIβ + GFP, n= 98 cells for si-PI(4)KIIIβ + MAPL-FLAG, n= 105 cells for si-Arf1 + GFP, n= 107 cells for si-Arf1 + MAPL-FLAG, n= 96 cells for si-Drp1 + GFP, n= 104 cells for si-Drp1 + MAPL-FLAG. Fig. S8D: n= 152 cells for si-NT + DMSO, n= 156 cells for si-NT + CCCP, n= 164 cells for si-PI(4)KIIIβ + DMSO, n= 157 cells for si-PI(4)KIIIβ + CCCP, n= 162 cells for si-Arf1 + DMSO, n= 154 cells for si-Arf1 + CCCP, n= 160 cells for si-Drp1 + DMSO, n= 159 cells for si-Drp1 + DMSO. Fig. S9B: n = 186, 156, 184, 154, 180, 168, 179, 165, 154, 156, 154, 155 cells for si-NT, si-PI(4)KIIIβ, si-SLP2, si-PI(4)KIIIβ + si-SLP2, si-Mfn1, si-PI(4)KIIIβ + si-Mfn1, si-Mfn2, si-PI(4)KIIIβ + si-Mfn2, si-Drp1, si-Drp1 + si-SLP2, si-Drp1 + si-Mfn1 and si-Drp1 + si-Mfn2, respectively. Fig. S10B-D: n = 60 cells. Fig. S10G-I: n = 60 cells. Fig. S12C: n = 90, 91, 90, 90 cells for si-NT, si-PI(4)KIIIβ, si-Arf1 and si-Drp1, respectively. Fig. S14B: n= 15 cells, 88 events (left panel) and n= 15 cells, 54 events (right panel).

Fig. S14D: n= 15 cells, 69 events (left panel) and n= 15 cells, 32 events (right panel). Fig. S14F: n= 15 cells, 35 events.

Quantification of Network diffusibility

Network diffusibility was calculated using the difference in the Mander's coefficient (quantifying co-localizing pixels) between the photo-activable mitochondria targeted pOCT-PA-GFP probe (*29*) and MTS-scarlet signals between t-0 and t-5 min post-photo-activation. Fiji software was used to measure Mander's coefficient and the difference between the two was calculated as the network diffusibility.

Heavy membranes isolation

Cells were washed once with cold PBS, and scraped over ice in Heavy Membranes Isolation Buffer (HMIB) (220 mM mannitol, 70 mM sucrose, 10 mM Hepes pH 7.5, 1 mM EGTA and Roche complete protease inhibitor cocktail). Cells were broken with manual tissue grind (Kimble). Samples were centrifuged at 800 x *g* for 10 min at 4°C. Post-nuclear supernatants were then centrifuged at 9,000 x *g* for 10 min at 4°C to pellet the heavy membranes fraction. Pellets were washed and re-centrifuged at 4°C for a further 15 min at 9,000 x *g*. The post-heavy membrane supernatants were then centrifuged at 100,000 x *g* at 4°C for 60 min to obtain the cytosolic fraction (supernatant). Total extracts, heavy membranes and cytosolic fractions were extracted with HMIB 1% Triton, normalized for protein content and processed for SDS-PAGE and immunoblotting.

Mitochondrial-associated membranes (MAM) isolation

MAM isolation was performed as described previously (*41*). Briefly, HeLa cells were trypsinized, pelleted at 300 x *g* and washed in PBS, pH 7.4. Pellets were resuspended in pre-chilled mitochondria isolation buffer (MIB) (220 mM mannitol, 70 mM sucrose, 10 mM Tris-KOH pH 7.4, 1 mM EDTA) with protein cocktail inhibitor and homogenized in a manual glass mortar (Kimble). Homogenates were centrifuged at 800 x *g*. Supernatants were centrifuged at 2,300 x *g* with pellets washed in MIB and collected as the crude mitochondrial fraction (CMF). Additional centrifugations at 9,000 x *g* were performed. Supernatants were then centrifuged at 100,000 x *g* for 60 min 4° C and cytosolic (supernatant) and microsomal (pellet) fractions were obtained. CMF was then resuspended in MIB buffer, layered on 30% Percoll solution and centrifuged at 95,000 x *g* for 65 min at 4°C. MAM and pure mitochondrial fractions (PMF) were extracted with 20-gauge needles. MAM and PMF were then washed in ice-cold PBS, pH 7.4 and centrifuged at 6,300 x *g* and 10,000 x *g* for 20 min for MAM and PMF, respectively. All fractions were extracted with MIB 1% Triton, normalized for protein content and processed for SDS-PAGE and Immunoblotting.

SDS-PAGE and Immunoblot

Cells were lysed in RIPA buffer (20 mM Tris pH 8.0, 150 mM NaCl, 0.1% SDS, 1% deoxycholic acid, 1% NP-40 and complete protease inhibitor cocktail). Samples were normalized for protein concentration using a Bio Rad protein assay (BioRad). Proteins were resolved by SDS-PAGE and transferred to nitrocellulose membranes (0.2 µm pore size, BioRad) or PVDF membrane (0.2 µm pore size, GE-Healthcare).

For immunoblot analysis, membranes were blocked with 5% non-fat milk or 5% BSA in PBS for 60 min at RT. Membranes were incubated with primary antibody at the appropriate dilution (in 2% milk or 2% BSA in 0.05% Tween-20 in PBS) at 4°C overnight. Membranes were washed in 0.05% tween in PBS 3 times for 15 min and incubated with appropriate secondary

antibodies (1/3,000 in 2% Milk or 2% BSA in 0.05% Tween-20 in PBS). Membranes were treated with Western Lightning Plus ECL (Perkin Elmer), and exposed to chemiluminescence either on films (PROTEC®) or on a digital ECL machine (Amersham) for image quantification. Immunoblots are representative of at least 3 biological replicates.

Quantitative RT-PCR

Total RNAs from control and silenced cells were isolated using the RNeasy kit (QIAGEN) and cDNA was synthesised using High-Capacity cDNA RT kit (Applied Biosystems) following manufacturers' instructions. mRNA levels were then quantified using the QuantStudio 3 Real-Time PCR system (Applied Biosystems).

The following pair of primers were used in HeLa cells: GAPDH: Forward (Fwd): 5'-GGTGAAGGTCGGAGTCAACG-3', Reverse (Rev): 5'-GAGGGATCTCGCTCCTGGAAG-3'; PI(4)KIIβ: Fwd : 5'-GAAGCGGGTGCCTATCTTGT-3', Rev: 5'-GGAACCAATCTTAGGAGG GAGT-3'. In Cos-7 cells: GAPDH: Fwd: 5'-GTGAAGGTCGGAGTCAACGG-3', Rev: 5'-GATTTTGGAGGGATCTCGTTCCT-3'; PI(4)KIIβ: Fwd: 5'-CGAAGCGGGTGCCTATTTTG-3', Rev: 5'-ACAAATAACTTAGGAGGGAGTCCT-3'.

Statistical analysis

For the bar graphs of mitochondrial morphology and qRT-PCR analysis, errors bars displayed on graphs represent the mean ± S.D from 3 independent experiments. For the bar graphs of live cell analysis, errors bars displayed on graphs represent the mean ± S.E.M from 3 independent experiments. For the boxplots, the boxes represent the 25th and 75th percentiles, the line is the median, and the whiskers represent the 10th and 90th percentiles from 3 independent experiments. Number of cells analysed are shown in supplementary methods. Statistical significance was analysed using one-way ANOVA, two-way ANOVA or unpaired t-test. All statistical analyses were performed using GraphPad Prism software. *$p < 0.05$, **$p < 0.01$, *** $p < 0.001$ and **** $p < 0.0001$ were considered significant. Statistical results, along with tests used, were summarized in Table S1.

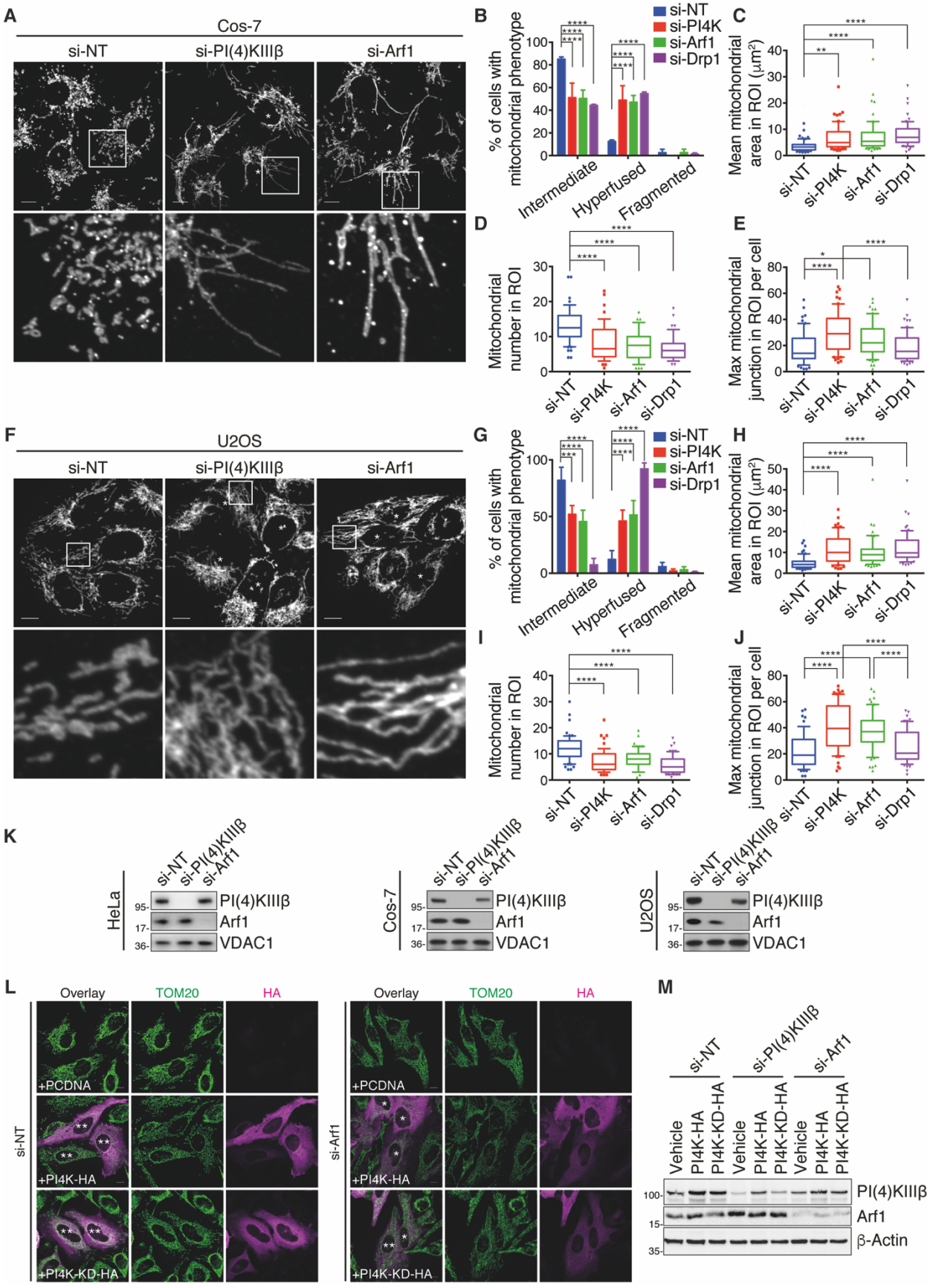
A
Cos-7
si-NT
si-PI(4)KIIIβ
si-Arf1
B
si-NT
si-PI4K
si-Arf1
si-Drp1
% of cells with mitochondrial phenotype
Intermediate
Hyperfused
Fragmented
C
Mean mitochondrial area in ROI (μm²)
D
Mitochondrial number in ROI
E
Max mitochondrial junction in ROI per cell
F
U2OS
G
H
I
J
K
HeLa
Cos-7
U2OS
PI(4)KIIIβ
Arf1
VDAC1
L
Overlay
TOM20
HA
+PCDNA
+PI4K-HA
+PI4K-KD-HA
M
Vehicle
PI4K-HA
PI4K-KD-HA
β-Actin

Fig. S1. Arf1 and PI(4)KIIIβ silencing leads to mitochondrial hyperfusion and branching. **(A)** Representative confocal images of mitochondrial morphology in Cos-7 cells treated with indicated siRNAs. Mitochondria were labelled using an anti-TOM20 antibody. * indicates cells with elongated/branched mitochondria. **(B)** Quantification of mitochondrial morphology from (A). **(C-E)** Mitochondrial morphology was quantified for **(C)** mean mitochondrial area per mitochondrion, **(D)** mitochondrial number, and **(E)** mitochondrial branching measured by maximum mitochondrial junction number, per region of interest (ROI). **(F)** Representative confocal images of mitochondrial morphology in U2OS cells treated with indicated siRNAs. Mitochondria were labelled using an anti-TOM20 antibody. * indicates cells with elongated/branched mitochondria. **(G)** Quantification of mitochondrial morphology from (F). **(H-J)** Mitochondrial morphology was quantified for (**H**) mean mitochondrial area per mitochondrion, **(I)** mitochondrial number, and **(J)** mitochondrial branching measured by maximum mitochondrial junction number, per region of interest (ROI). **(K)** Immunoblot analysis showing the efficiency of the PI(4)KIIIβ and Arf1 siRNAs at 3 and 2 days, respectively, in HeLa (left panel), Cos-7 (middle panel), and U2OS (right panel). **(L)** Representative confocal images of mitochondrial morphology in NT- and Arf1-silenced HeLa cells transiently expressing empty vector (vehicle), WT-PI(4)KIIIβ-HA (PI4K-HA) and kinase-dead mutant PI(4)KIIIβ-HA (PI4K-KD-HA). * and ** indicate HA-positive transfected cells with * elongated/branched mitochondria and ** intermediate mitochondria. **(M)** Immunoblot analysis showing the efficiency of the WT-PI(4)KIIIβ-HA and PI(4)KIIIβ-KD-HA transfections in HeLa cells silenced with indicated siRNAs. All scale bars: 10 μm. All values: mean ± SD; at least three independent experiments; (B, G): two-way ANOVA, Tukey's multiple comparisons test; (C-E, H-J): ordinary one-way ANOVA, Tukey's multiple comparisons test.

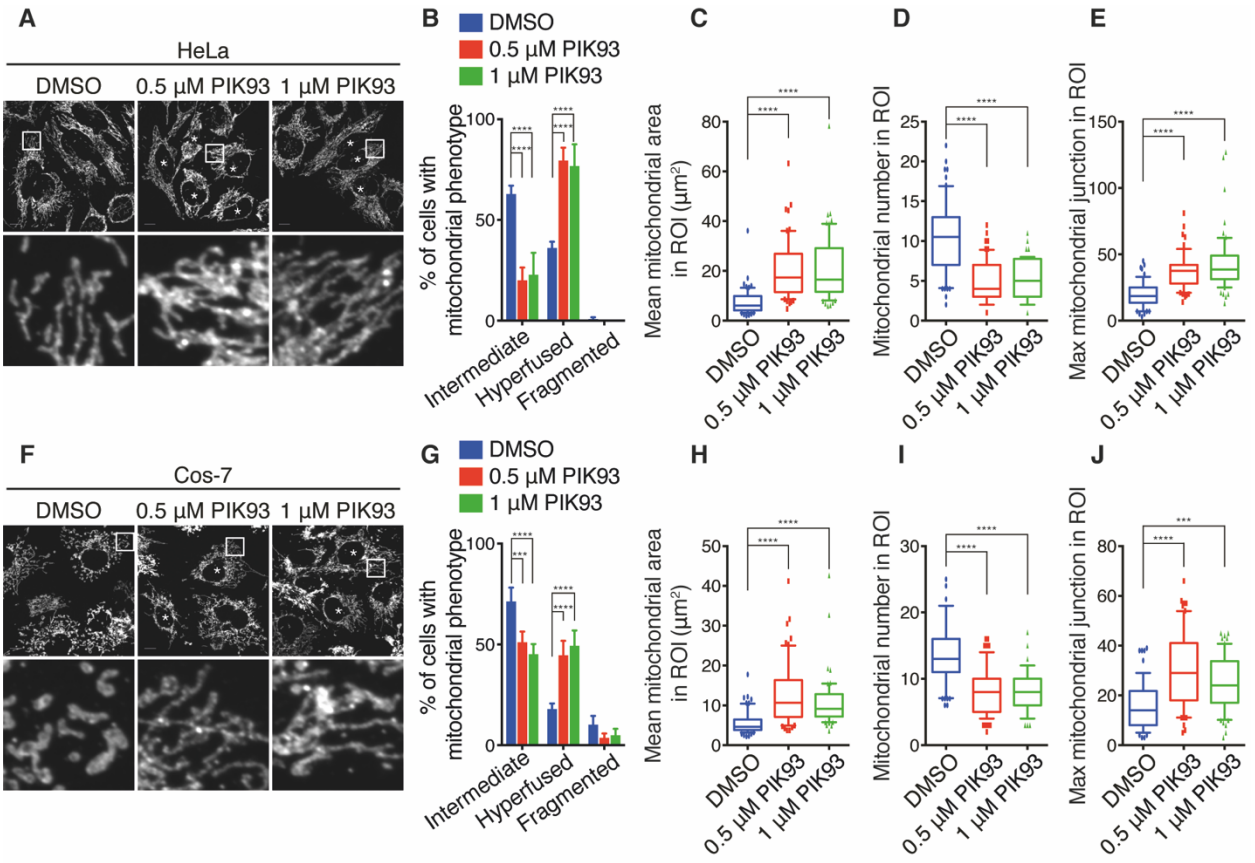

Fig. S2. PI(4)KIIIβ inhibitor induces mitochondrial hyperfusion and branching.
(A) Representative confocal images of mitochondrial morphology in HeLa cells treated with the PI(4)KIIIβ inhibitor, PIK93, for 24 hours (hr) at indicated concentrations. Mitochondria were labelled using an anti-TOM20 antibody. * indicates cells with elongated/branched mitochondria. **(B)** Quantification of mitochondrial morphology from (A). **(C-E)** Mitochondrial morphology was quantified for **(C)** mean mitochondrial area per mitochondrion, **(D)** mitochondrial number, and **(E)** mitochondrial branching measured by maximum mitochondrial junction number, per region of interest (ROI). **(F)** Representative confocal images of mitochondrial morphology in Cos-7 cells treated with the PI(4)KIIIβ inhibitor, PIK93, for 24 hr at indicated concentrations. Mitochondria were labelled using an anti-TOM20 antibody. * indicates cells with elongated/branched mitochondria. **(G)** Quantification of mitochondrial morphology from (F). **(H-J)** Mitochondrial morphology was quantified for **(H)** mean mitochondrial area per mitochondrion, **(I)** mitochondrial number, and **(J)** mitochondrial branching measured by maximum mitochondrial junction number, per region of interest (ROI). All values: mean ± SD; at least three independent experiments; (B, G): two-way ANOVA, Tukey's multiple comparisons test; (C-E, H-J): ordinary one-way ANOVA, Tukey's multiple comparisons test.

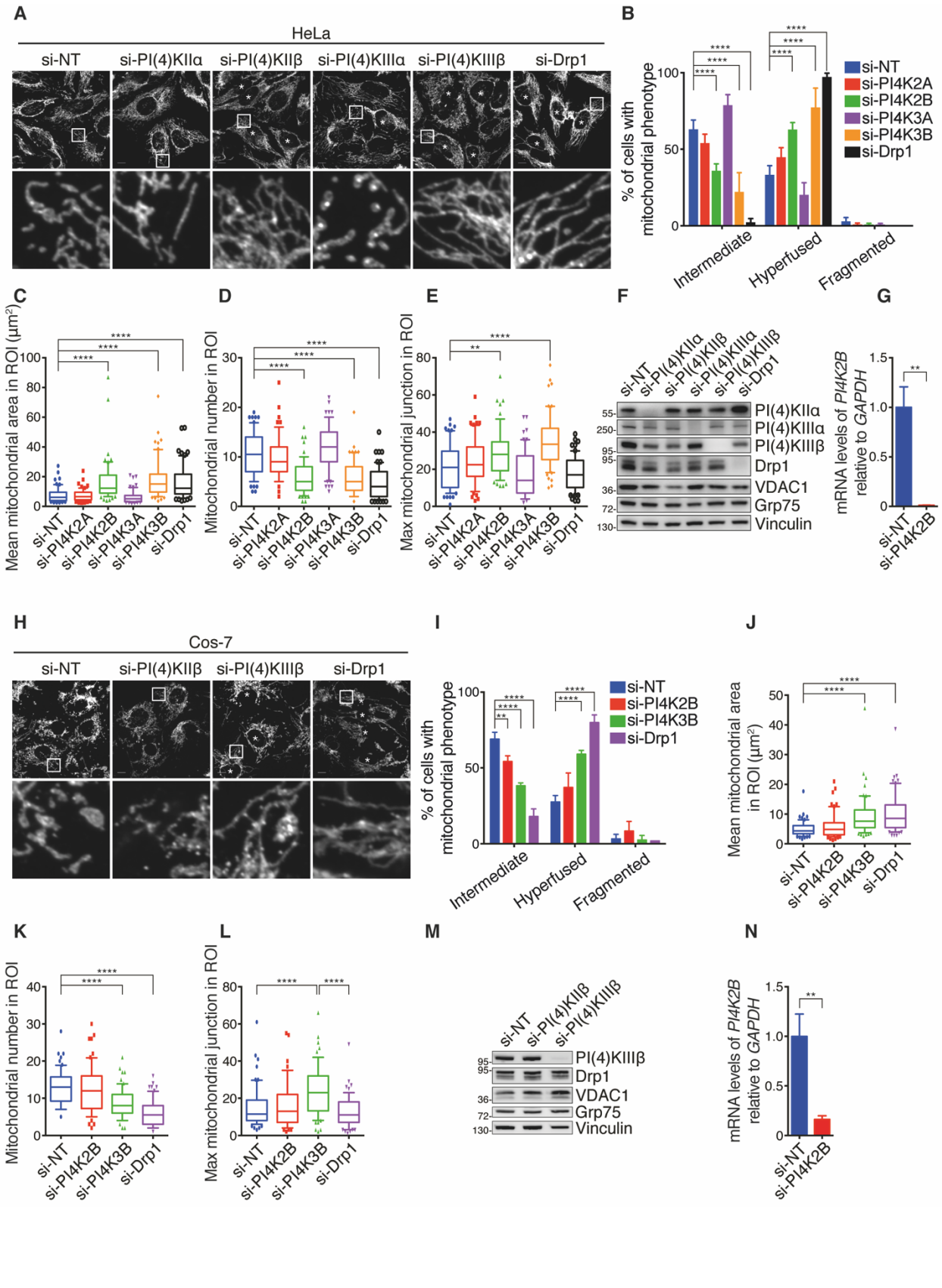
A
HeLa
si-NT
si-PI(4)KIIα
si-PI(4)KIIβ
si-PI(4)KIIIα
si-PI(4)KIIIβ
si-Drp1
B
% of cells with mitochondrial phenotype
si-NT
si-PI4K2A
si-PI4K2B
si-PI4K3A
si-PI4K3B
si-Drp1
Intermediate
Hyperfused
Fragmented
C
Mean mitochondrial area in ROI (μm²)
D
Mitochondrial number in ROI
E
Max mitochondrial junction in ROI
F
PI(4)KIIα
PI(4)KIIIα
PI(4)KIIIβ
Drp1
VDAC1
Grp75
Vinculin
G
mRNA levels of PI4K2B relative to GAPDH
H
Cos-7
I
J
K
L
M
N

Fig. S3. Specific loss of PI(4)KIIIβ induces mitochondrial hyperfusion and branching.
(A) Representative confocal images of mitochondrial morphology in HeLa cells treated with indicated siRNAs. Mitochondria were labelled using an anti-TOM20 antibody. * indicates cells with elongated/branched mitochondria. **(B)** Quantification of mitochondrial morphology from (A). **(C-E)** Mitochondrial morphology was quantified for **(C)** mean mitochondrial area per mitochondrion, **(D)** mitochondrial number, and **(E)** mitochondrial branching measured by maximum mitochondrial junction number, per region of interest (ROI). **(F)** Immunoblot analysis showing the efficiency of the indicated siRNAs at 3 days in HeLa cells. **(G)** Quantification of *PI(4)KIIβ* mRNA levels in HeLa silenced cells by qRT-PCR normalized to *GAPDH* mRNA and expressed relative to control cells. **(H)** Representative confocal images of mitochondrial morphology in Cos-7 cells treated with indicated siRNAs. Mitochondria were labelled using an anti-TOM20 antibody. * indicates cells with elongated/branched mitochondria. **(I)** Quantification of mitochondrial morphology from (H). **(J-L)** Mitochondrial morphology was quantified for **(J)** mean mitochondrial area per mitochondrion, **(K)** mitochondrial number, and **(L)** mitochondrial branching measured by maximum mitochondrial junction number, per region of interest (ROI).
(M) Immunoblot analysis showing Drp1 and PI(4)KIIIβ levels upon silencing with the indicated siRNAs at 3 days in Cos-7 cells. **(N)** Quantification of *PI(4)KIIβ* mRNA levels in Cos-7 silenced cells by qRT-PCR normalized to *GAPDH* mRNA and expressed relative to control cells. All scale bars: 10 μm. All values: mean ± SD; at least three independent experiments; (B, I): two-way ANOVA, Tukey's multiple comparisons test; (C-E, J-L): ordinary one-way ANOVA, Tukey's multiple comparisons test; (G, N): two-tailed unpaired student's t-test.

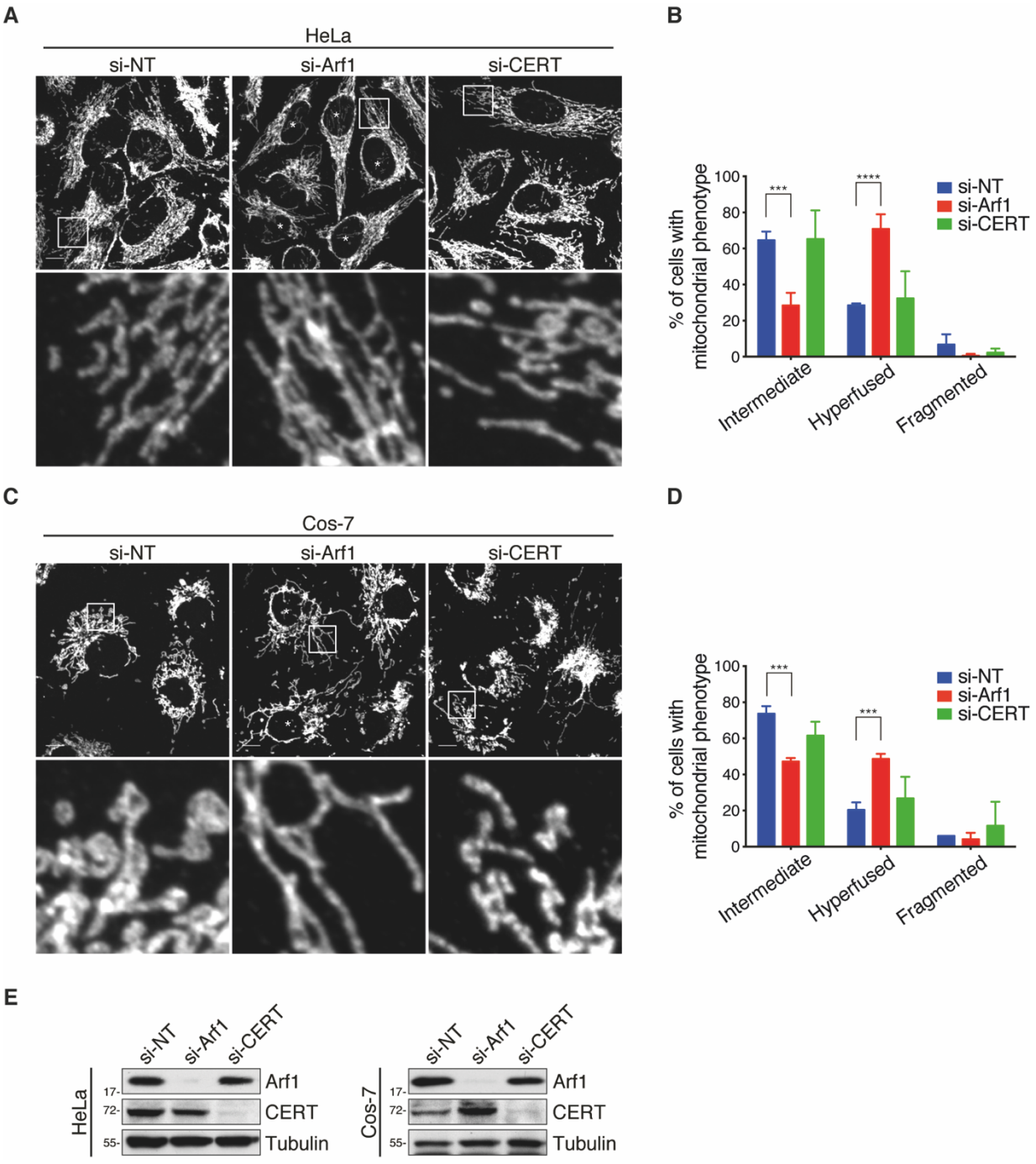

Fig. S4. Silencing of the Arf1 effector ceramide transfer protein (CERT) does not induce mitochondrial hyperfusion or branching.

(A) Representative confocal images of mitochondrial morphology in HeLa cells treated with indicated siRNAs. Mitochondria were labelled using an anti-TOM20 antibody. * indicates cells with elongated/branched mitochondria. **(B)** Quantification of mitochondrial morphology from (A). **(C)** Representative confocal images of mitochondrial morphology in Cos-7 cells treated with

indicated siRNAs. Mitochondria were labelled using an anti-TOM20 antibody. * indicates cells with elongated/branched mitochondria. **(D)** Quantification of mitochondrial morphology from (C). **(E)** Immunoblot analysis showing the efficiency of Arf1 and CERT siRNAs at 2 and 3 days, respectively, in HeLa (left panel) and Cos-7 (right panel) cells. All scale bars: 10 μm. All values: mean ± SD; at least three independent experiments; two-way ANOVA, Tukey's multiple comparisons test.

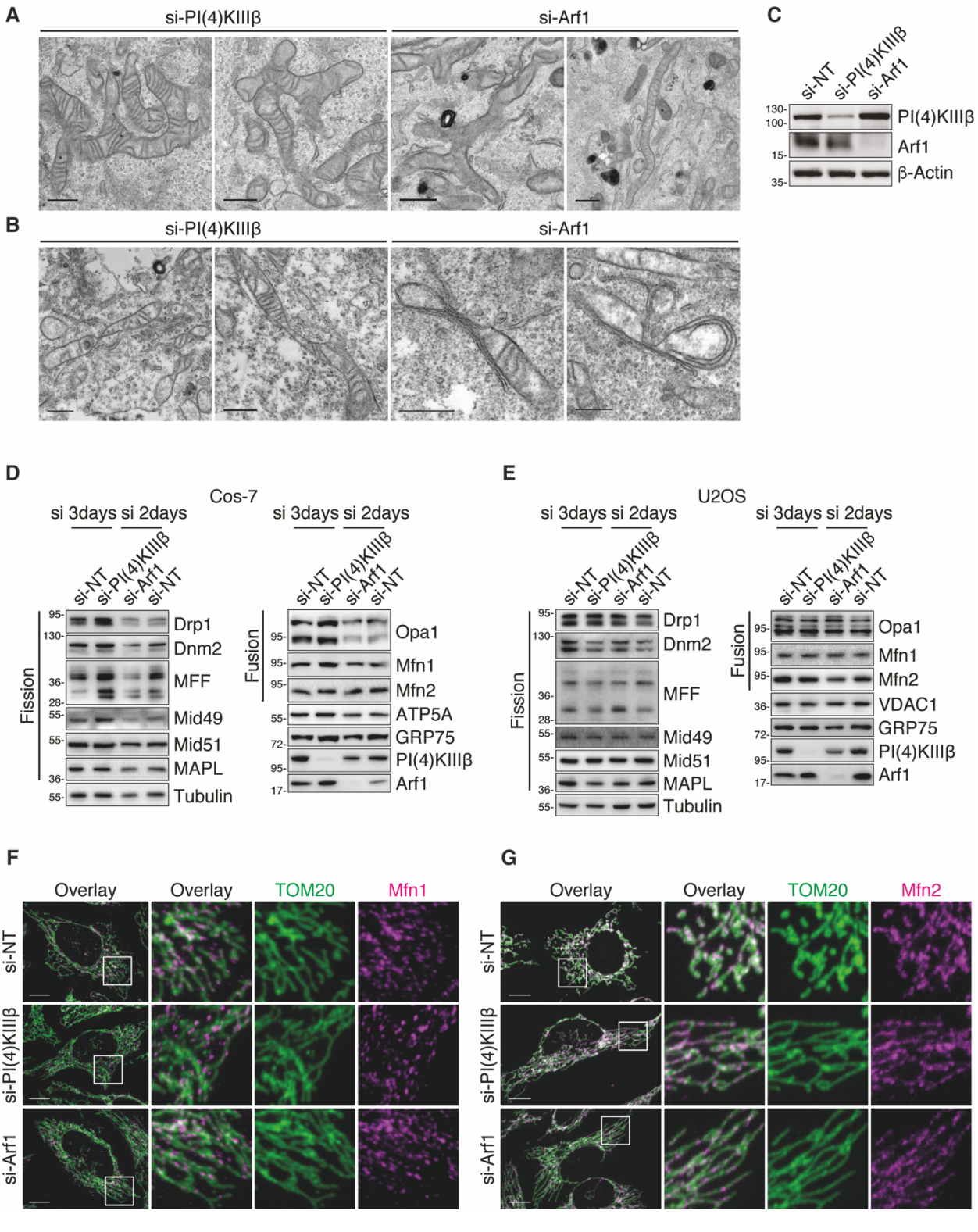
A
si-PI(4)KIIIβ
si-Arf1
B
si-PI(4)KIIIβ
si-Arf1
C
si-NT
si-PI(4)KIIIβ
si-Arf1
130-
100-
PI(4)KIIIβ
15-
Arf1
35-
β-Actin
D
Cos-7
si 3days si 2days
si-NT
si-PI(4)KIIIβ
si-Arf1
si-NT
Fission
95-
130-
Drp1
Dnm2
36-
28-
MFF
55-
Mid49
55-
Mid51
36-
MAPL
55-
Tubulin
Fusion
95-
Opa1
95-
Mfn1
95-
Mfn2
55-
ATP5A
72-
GRP75
95-
PI(4)KIIIβ
17-
Arf1
E
U2OS
si 3days si 2days
si-NT
si-PI(4)KIIIβ
si-Arf1
si-NT
Fission
95-
130-
Drp1
Dnm2
36-
28-
MFF
55-
Mid49
55-
Mid51
36-
MAPL
55-
Tubulin
Fusion
95-
Opa1
95-
Mfn1
95-
Mfn2
36-
VDAC1
72-
GRP75
95-
PI(4)KIIIβ
17-
Arf1
F
Overlay
Overlay
TOM20
Mfn1
si-NT
si-PI(4)KIIIβ
si-Arf1
G
Overlay
Overlay
TOM20
Mfn2
si-NT
si-PI(4)KIIIβ
si-Arf1

Fig. S5. The fission/fusion proteins are not altered upon silencing of PI(4)KIIIβ and Arf1.
(A-B) Other examples of representative transmission electron microscopy (TEM) images of cells treated with PI(4)KIIIβ (left panels) and Arf1 (right panels) siRNAs, showing **(A)** branched mitochondria and **(B)** mitochondrial super-constriction sites. Scale bars: 500 nm. **(C)** Immunoblot analysis showing the efficiency of the indicated siRNAs in HeLa cells used for TEM experiments in Fig. 2A and in Fig. S5 (A-B). **(D-E)** Levels of proteins relevant to mitochondrial fission (left panels) and fusion (right panels) from **(D)** Cos-7 and **(E)** U2OS cells, treated with indicated siRNAs. **(F-G)** Representative confocal images of NT-, PI(4)KIIIβ- and Arf1-silenced HeLa cells with mitochondria and **(F)** Mfn1, and **(G)** Mfn2 labelled. Scale bars: 10 μm.

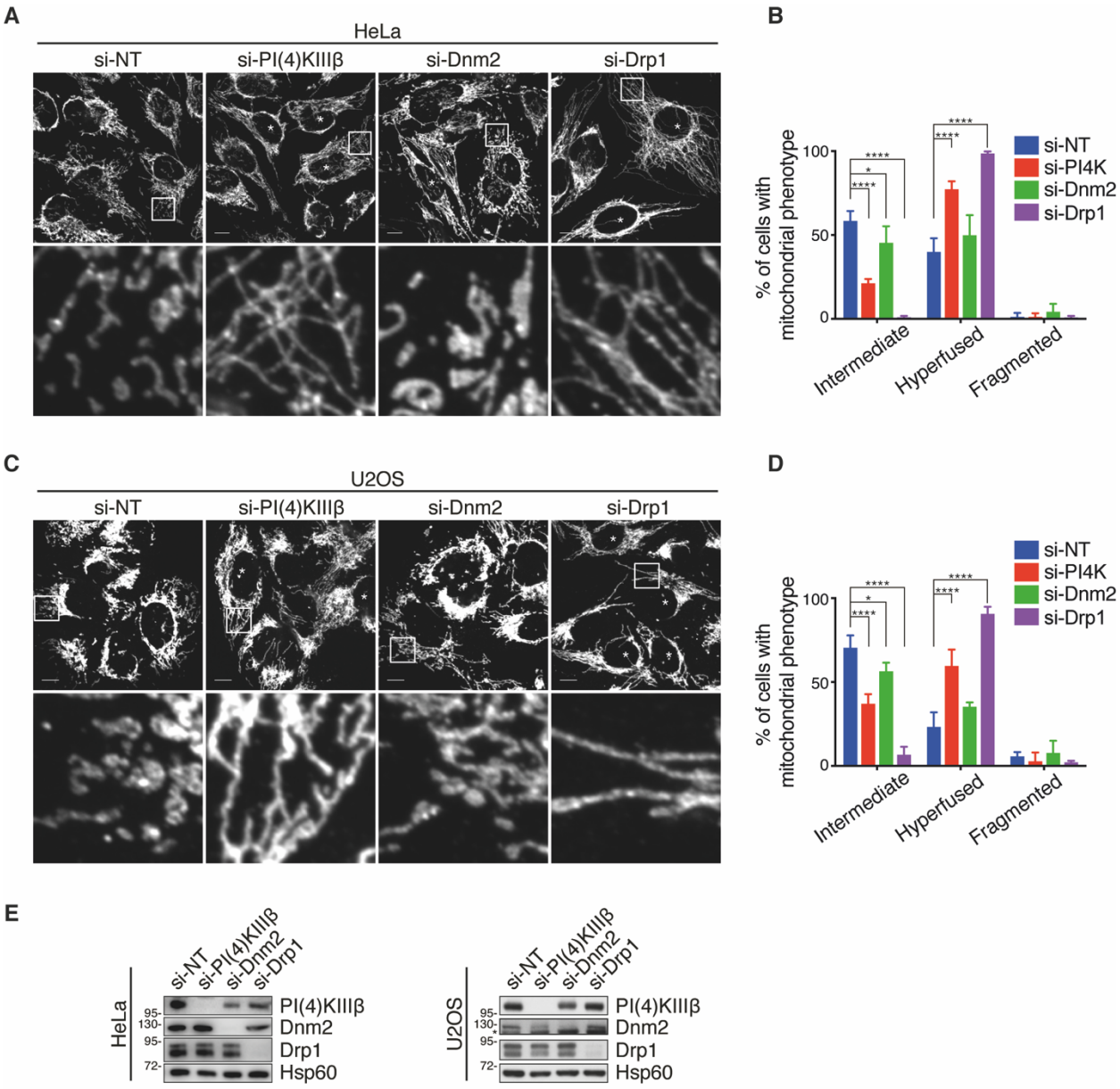

Fig. S6. Silencing of Dynamin 2 (Dnm2) does not phenocopy the loss of PI(4)P pools.
(A, C) Representative confocal images of mitochondrial morphology in **(A)** HeLa and **(C)** U2OS cells treated with indicated siRNAs. Mitochondria were labelled using an anti-TOM20 antibody. * indicates cells with elongated/branched mitochondria. **(B, D)** Quantification of mitochondrial morphology from (A) and (C), respectively. **(E)** Immunoblot analysis showing the efficiency of the indicated siRNAs at 3 days in HeLa (left panel) and U2OS (right panel) cells. * indicates unspecific bands. All values: mean ± SD; at least three independent experiments; two-way ANOVA, Tukey's multiple comparisons test.

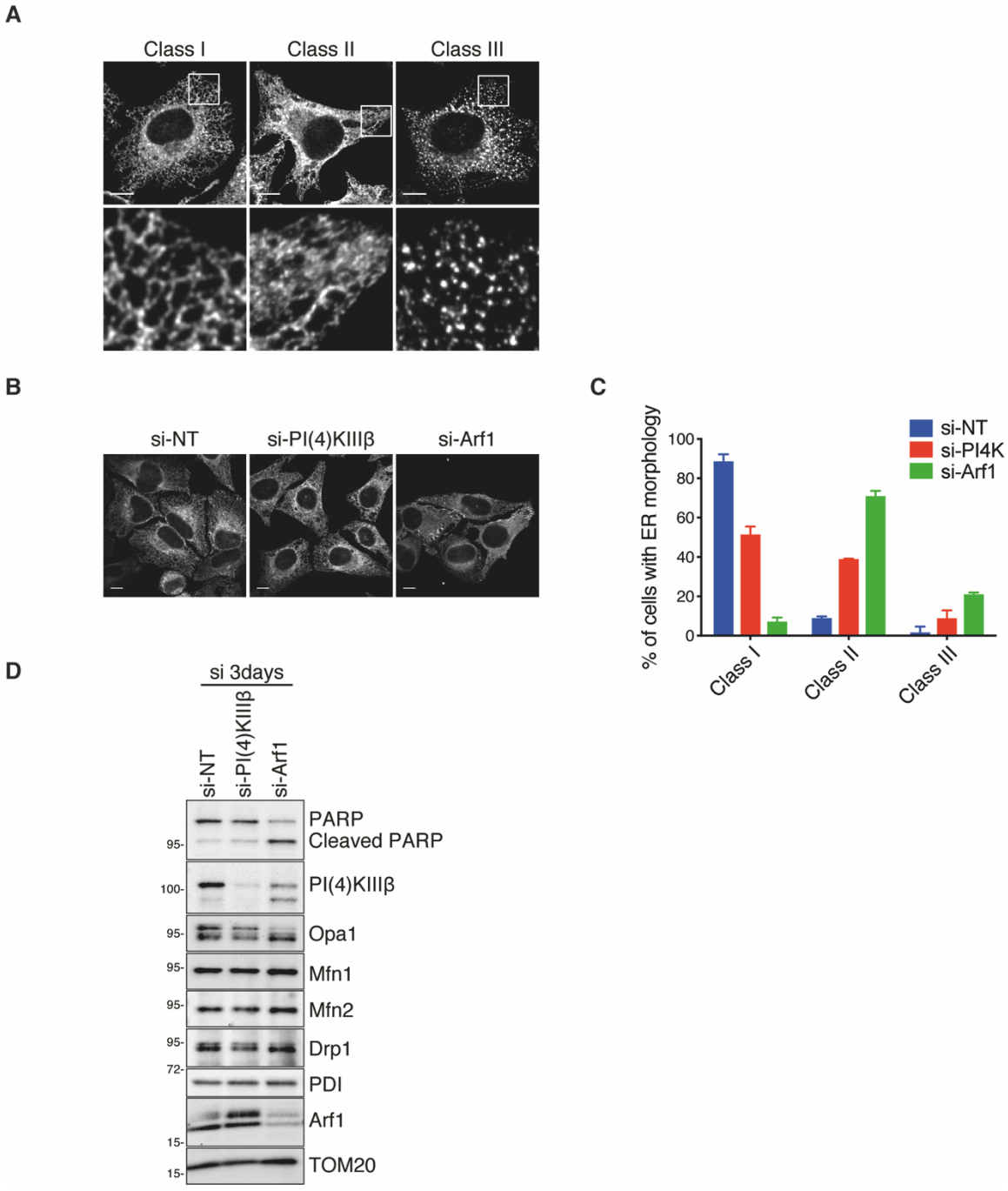

Fig. S7. Silencing Arf1 for 3 days induces ER morphology defects and cell death.
(A) Classification of the endoplasmic reticulum (ER) network organization stained with anti-KDEL antibody; classified as class I (normal), class II (disorganized) or class III (highly disorganized). **(B)** Representative confocal images of the ER network in HeLa cells treated with indicated siRNAs for 3 days. **(C)** Quantification of the ER morphology from (B). **(D)** Immunoblot analysis of proteins related to fission/fusion and apoptosis from HeLa cells treated with indicated siRNAs for 3 days. All scale bars: 10 μm. All values: mean ± SD; at least two independent experiments.

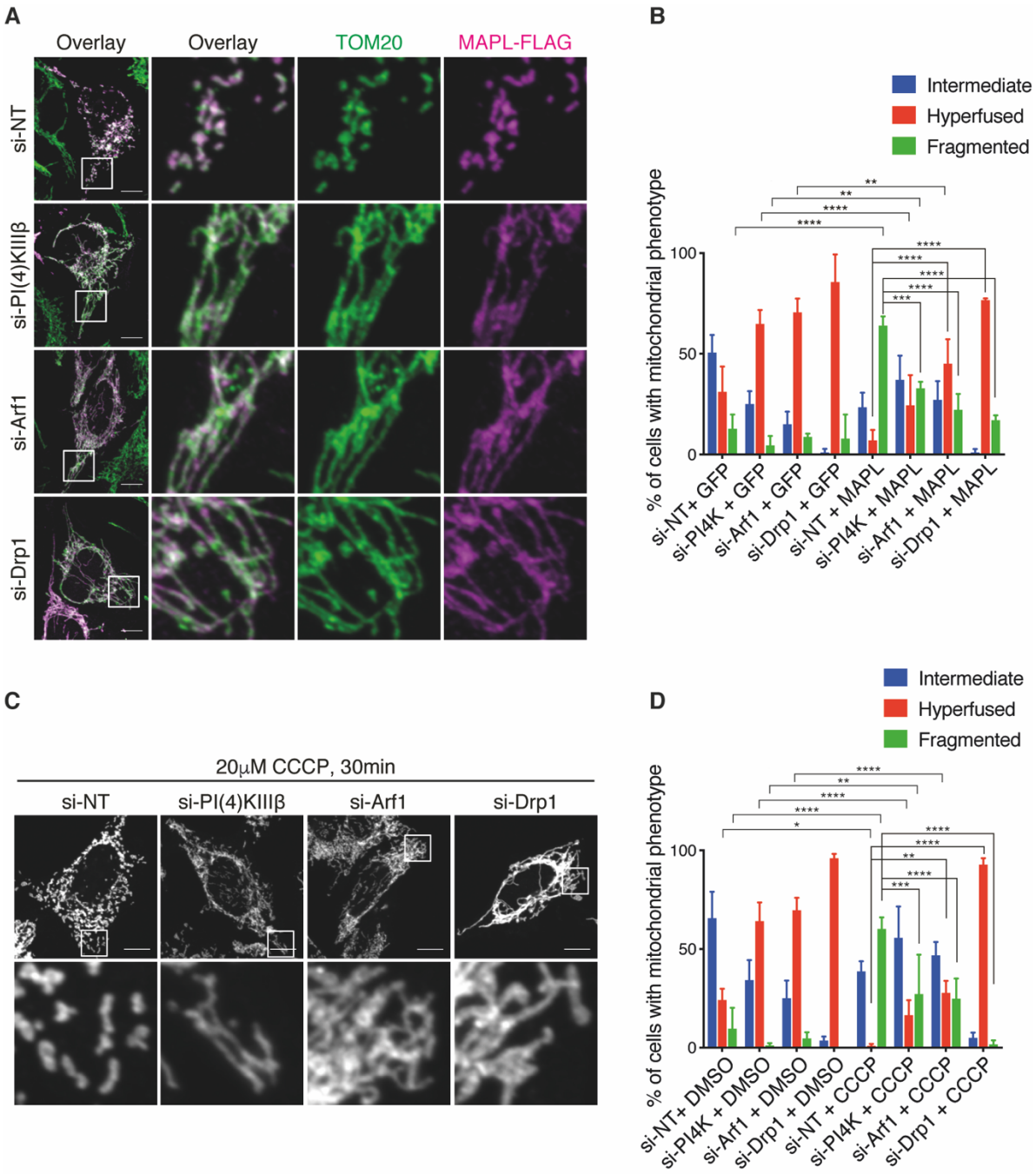

Fig. S8. Loss of PI(4)KIIIβ and Arf1 protects from stimulated mitochondrial division Drp1-dependent.

(A) Representative confocal images of mitochondrial morphology in NT-, PI(4)KIIIβ-, Arf1- and Drp1-silenced HeLa cells transiently expressing empty vector (vehicle) and MAPL-FLAG. Mitochondria were labelled using an anti-TOM20 antibody. **(B)** Quantification of mitochondrial morphology from (A). **(C)** Representative confocal images of mitochondrial morphology in NT-, PI(4)KIIIβ-, Arf1- and Drp1-silenced HeLa cells treated with 20 μM CCCP for 30 min. Mitochondria were labelled using an anti-TOM20 antibody. **(D)** Quantification of mitochondrial

morphology from (C). All scale bars: 10 μm. All values: mean ± SD; at least three independent experiments; two-way ANOVA, Tukey's multiple comparisons test.

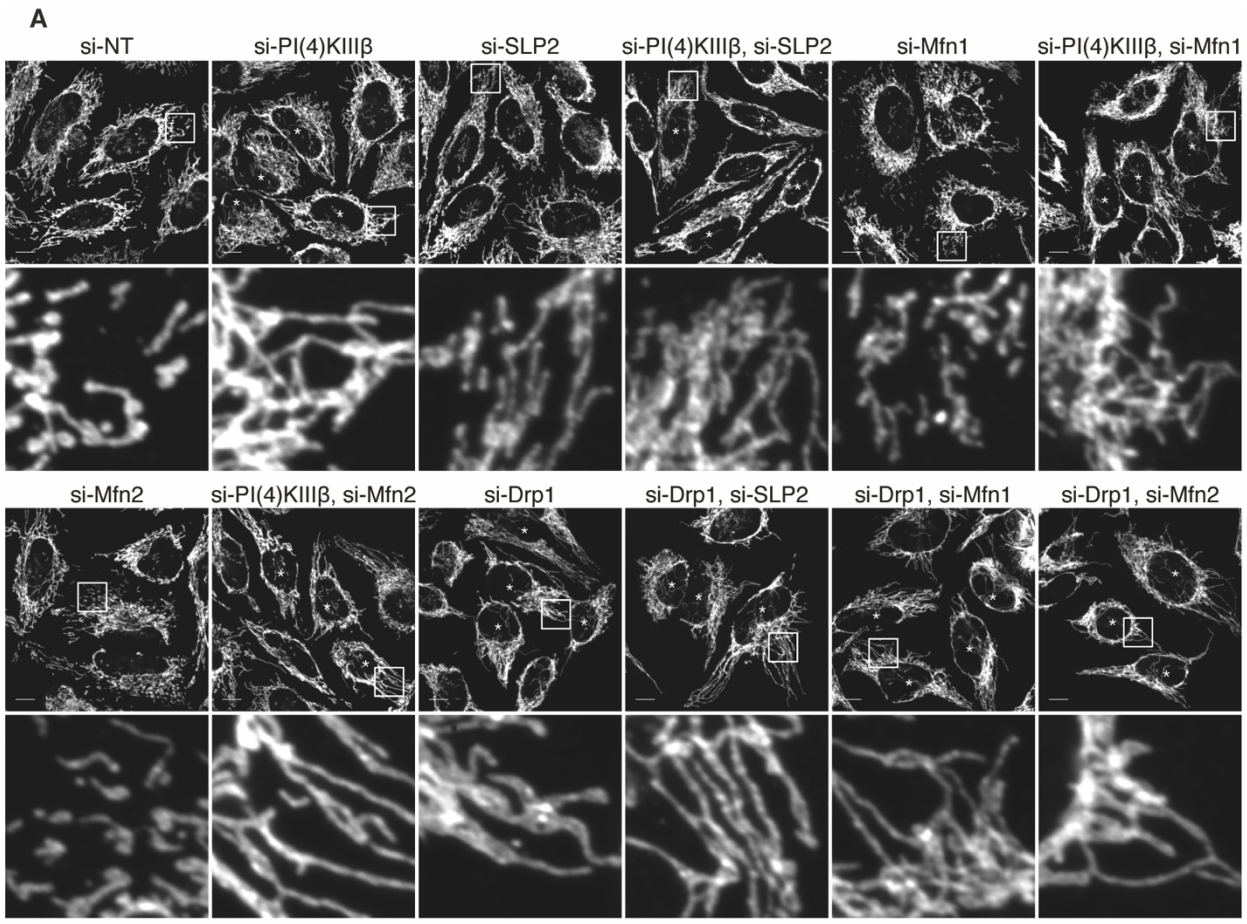
A
si-NT
si-PI(4)KIIIβ
si-SLP2
si-PI(4)KIIIβ, si-SLP2
si-Mfn1
si-PI(4)KIIIβ, si-Mfn1
si-Mfn2
si-PI(4)KIIIβ, si-Mfn2
si-Drp1
si-Drp1, si-SLP2
si-Drp1, si-Mfn1
si-Drp1, si-Mfn2

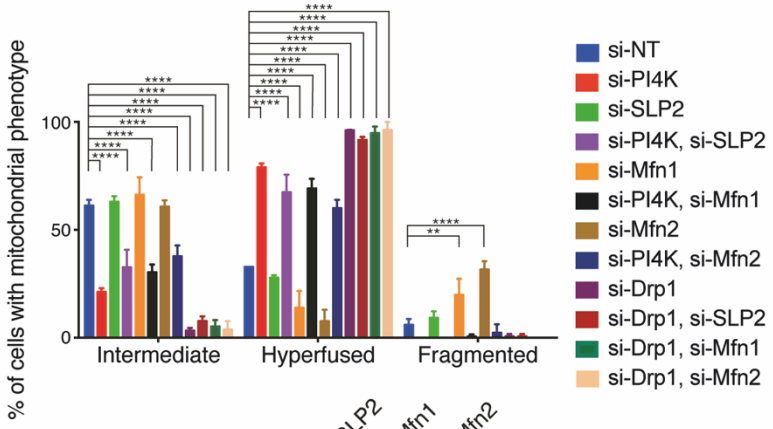
B
% of cells with mitochondrial phenotype
100
50
0
Intermediate
Hyperfused
Fragmented
si-NT
si-PI4K
si-SLP2
si-PI4K, si-SLP2
si-Mfn1
si-PI4K, si-Mfn1
si-Mfn2
si-PI4K, si-Mfn2
si-Drp1
si-Drp1, si-SLP2
si-Drp1, si-Mfn1
si-Drp1, si-Mfn2

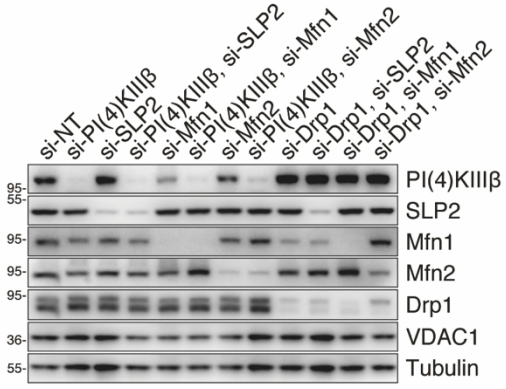
C
si-NT
si-PI(4)KIIIβ
si-SLP2
si-PI(4)KIIIβ, si-SLP2
si-Mfn1
si-PI(4)KIIIβ, si-Mfn1
si-Mfn2
si-PI(4)KIIIβ, si-Mfn2
si-Drp1
si-Drp1, si-SLP2
si-Drp1, si-Mfn1
si-Drp1, si-Mfn2
PI(4)KIIIβ
SLP2
Mfn1
Mfn2
Drp1
VDAC1
Tubulin

Fig. S9. Mitochondrial elongation induced by the loss of PI(4)KIIIβ and Arf1 is independent of stress-induced hyperfusion and increased mitochondrial fusion.
(A) Representative confocal images of mitochondrial morphology in HeLa cells treated with indicated siRNAs. Mitochondria were labelled using an anti-TOM20 antibody. * indicates cells with elongated/branched mitochondria. Scale bars: 10 μm. **(B)** Quantification of mitochondrial morphology from (A). **(C)** Immunoblot analysis showing the efficiency of the indicated siRNAs at 3 days in HeLa cells. All values: mean ± SD; at least three independent experiments; two-way ANOVA, Tukey's multiple comparisons test.

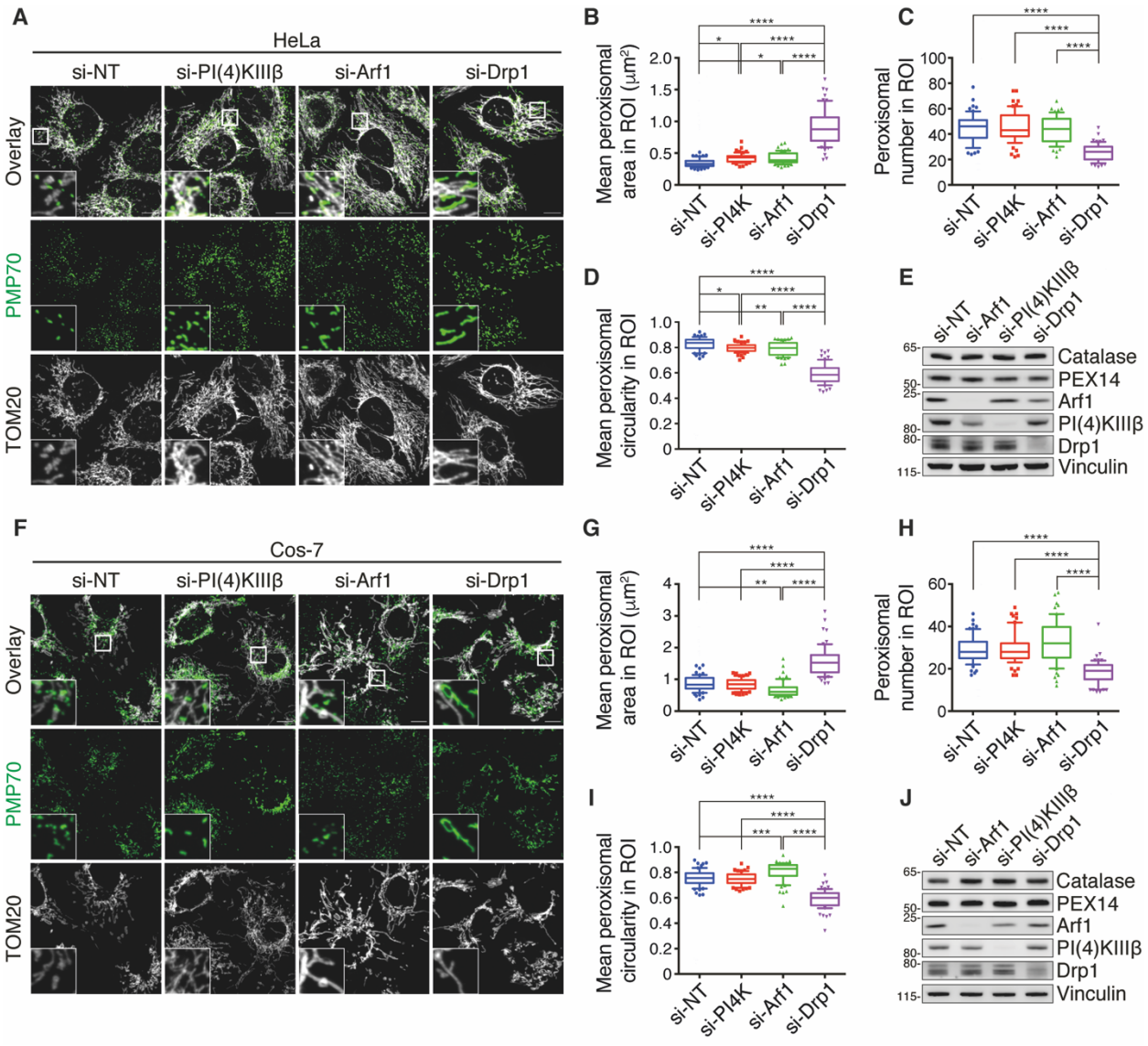

Fig. S10. Loss of PI(4)KIIIβ and Arf1 does not lead to peroxisome elongation.
(A) Representative confocal images of peroxisome morphology in HeLa cells treated with indicated siRNAs. Mitochondria and peroxisomes were labelled using an anti-TOM20 and anti-PMP70 antibodies, respectively. **(B-D)** Peroxisomes morphology was quantified for **(B)** mean peroxisomal area per peroxisome, **(C)** peroxisomal number, and **(D)** mean peroxisomal circularity, per region of interest (ROI). **(E)** Immunoblot analysis showing the efficiency of the PI(4)KIIIβ/Drp1 and Arf1 siRNAs at 3 and 2 days, respectively, in HeLa cells. **(F)** Representative confocal images of peroxisome morphology in Cos-7 cells treated with indicated siRNAs. Mitochondria and peroxisomes were labelled using an anti-TOM20 and anti-PMP70 antibodies, respectively. **(G-I)** Peroxisomes morphology was quantified for **(G)** mean peroxisomal area per peroxisome, **(H)** peroxisomal number, and **(I)** mean peroxisomal circularity, per region of interest (ROI). **(J)** Immunoblot analysis showing the efficiency of the PI(4)KIIIβ/Drp1 and Arf1 siRNAs at 3 and 2 days, respectively, in Cos-7 cells. All scale bars: 10 μm. Ordinary one-way ANOVA, Tukey's multiple comparisons test; three independent experiments.

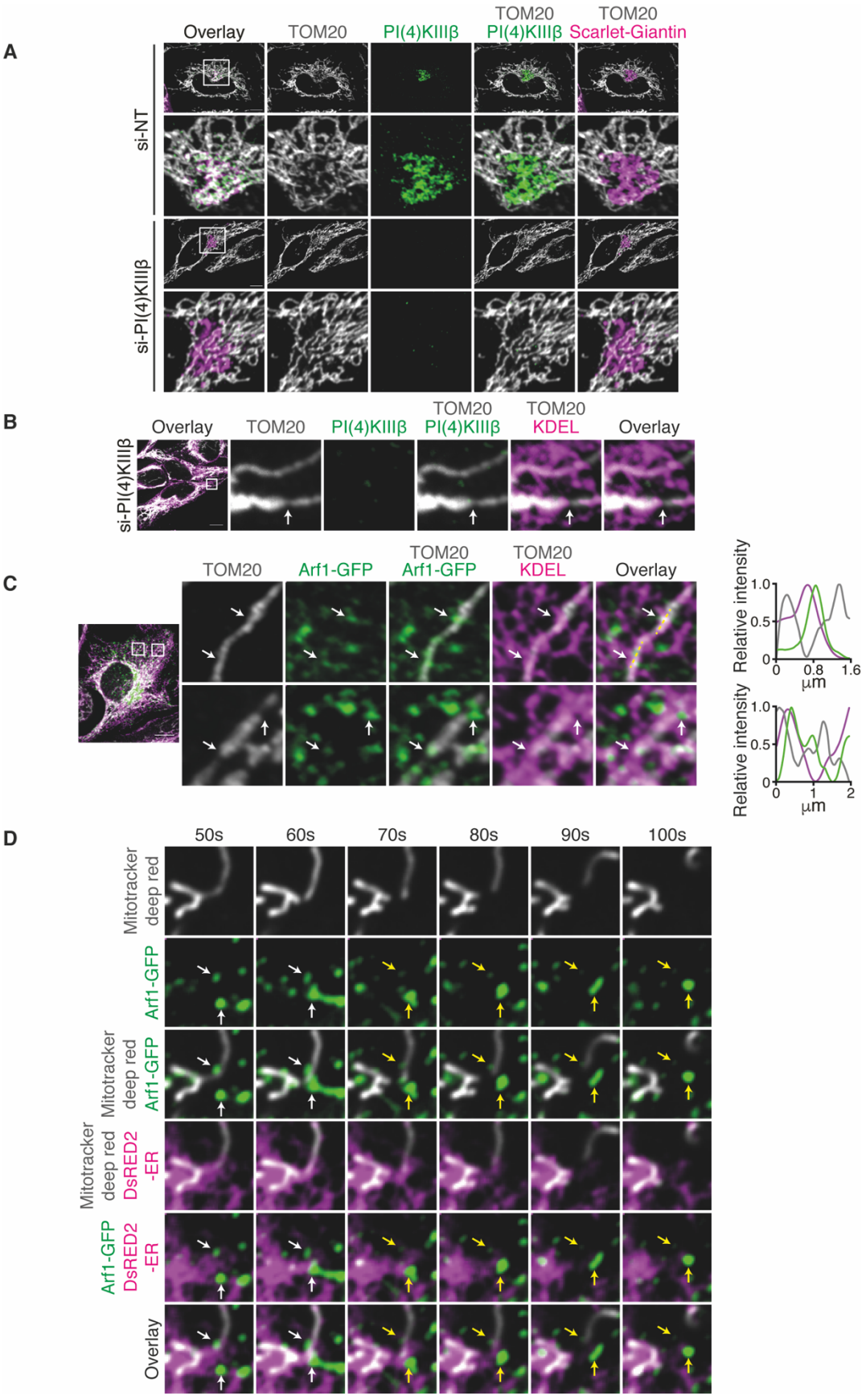
A
Overlay
TOM20
PI(4)KIIIβ
TOM20 PI(4)KIIIβ
TOM20 Scarlet-Giantin
si-NT
si-PI(4)KIIIβ
B
Overlay
TOM20
PI(4)KIIIβ
TOM20 PI(4)KIIIβ
TOM20 KDEL
Overlay
si-PI(4)KIIIβ
C
TOM20
Arf1-GFP
TOM20 Arf1-GFP
TOM20 KDEL
Overlay
Relative intensity
1.0
0.5
0
0
0.8
1.6
μm
Relative intensity
1.0
0.5
0
0
1
2
μm
D
50s
60s
70s
80s
90s
100s
Mitotracker deep red
Arf1-GFP
Mitotracker deep red Arf1-GFP
Mitotracker deep red DsRED2 -ER
Arf1-GFP DsRED2 -ER
Overlay

Fig. S11. Subcellular localization analysis of PI(4)KIIIβ and Arf1-GFP.
(A) Representative confocal images of NT- and PI(4)KIIIβ-silenced HeLa cells transiently expressing the Golgi apparatus marker, Scarlet-Giantin. **(B)** Representative confocal images of HeLa cells silenced for PI(4)KIIIβ. White arrows indicate mitochondria constriction at ER contacts. **(C)** Representative confocal images of HeLa cells transfected with Arf1-GFP showing Arf1-GFP foci at mitochondrial constriction sites and ER contacts localization (white arrows). Line-scan analysis (right panels) of relative fluorescence intensity from the dashed line are shown. **(D)** Confocal time lapse imaging of HeLa cells transiently expressing Arf1-GFP, ER-dsRED2 with mitochondria labelled using Mitotracker deep red. White and yellow arrows indicate Arf1-GFP puncta prior and after a fission event, respectively. All scale bars: 10 μm.

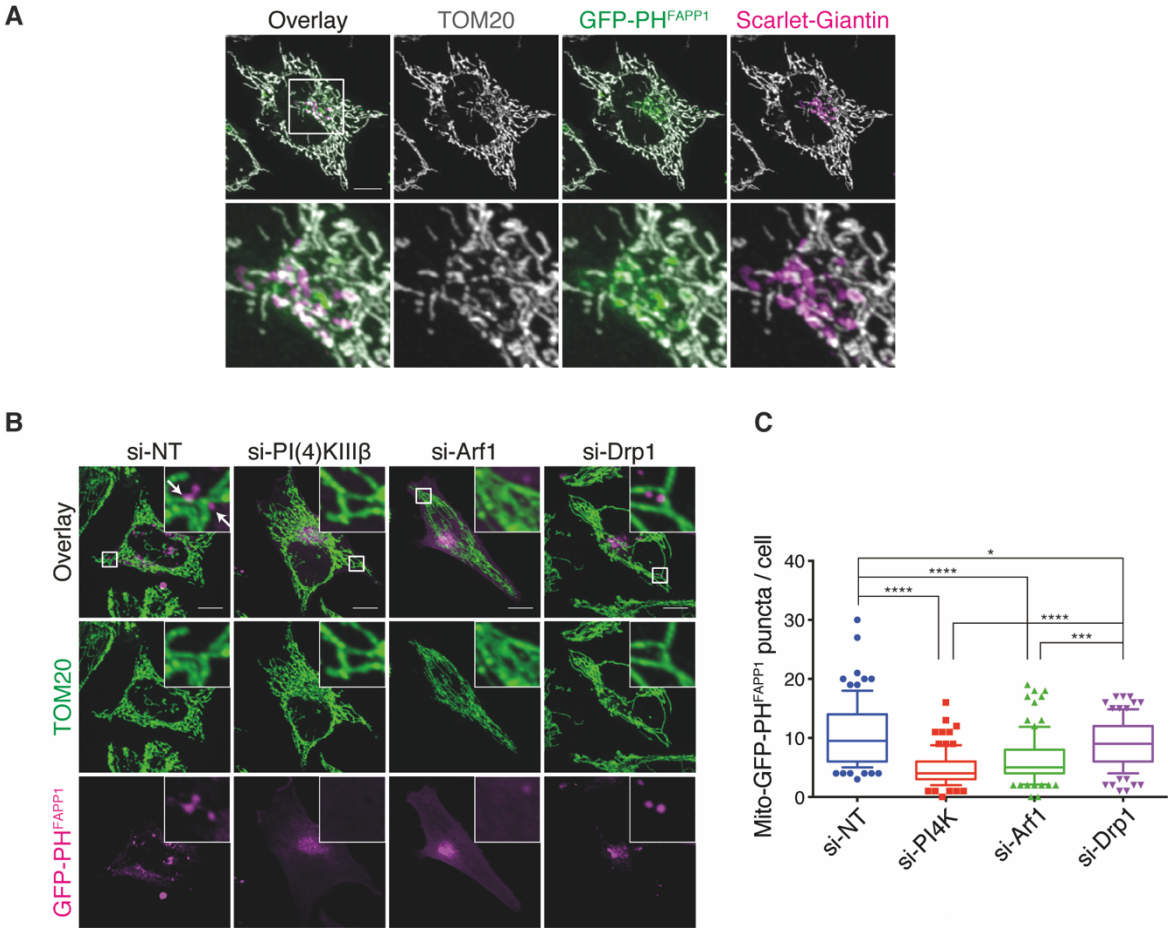

Fig. S12. GFP-PH^{FAPP1} foci crossing mitochondria are dependent of PI(4)KIIIβ, Arf1 and Drp1.

(A) Representative confocal images of HeLa cells transiently expressing GFP-PH^{FAPP1} and the Golgi apparatus marker, Scarlet-Giantin. **(B)** Representative confocal images of PI(4)KIIIβ-, Arf1- and Drp1-silenced HeLa cells transiently expressing GFP-PH^{FAPP1}. White Arrows indicate GFP-PH^{FAPP1} puncta associated to mitochondria. **(C)** Quantification of GFP-PH^{FAPP1} puncta associated to mitochondria from (B). All scale bars: 10 µm. Ordinary one-way ANOVA, Tukey's multiple comparisons test; three independent experiments.

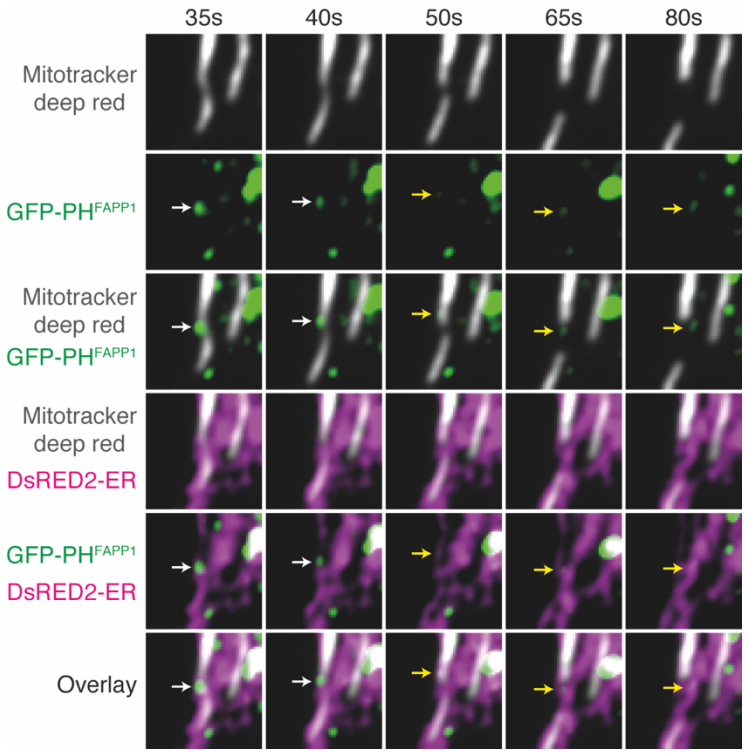

Fig. S13. GFP-PH^{FAPP1} foci are recruited to MERC during mitochondrial division.
Confocal time lapse imaging of HeLa cells transiently expressing GFP-PH^{FAPP1}, ER-dsRED2 with mitochondria labelled using Mitotracker deep red. White and yellow arrows indicate GFP-PH^{FAPP1} puncta prior and after a fission event, respectively.

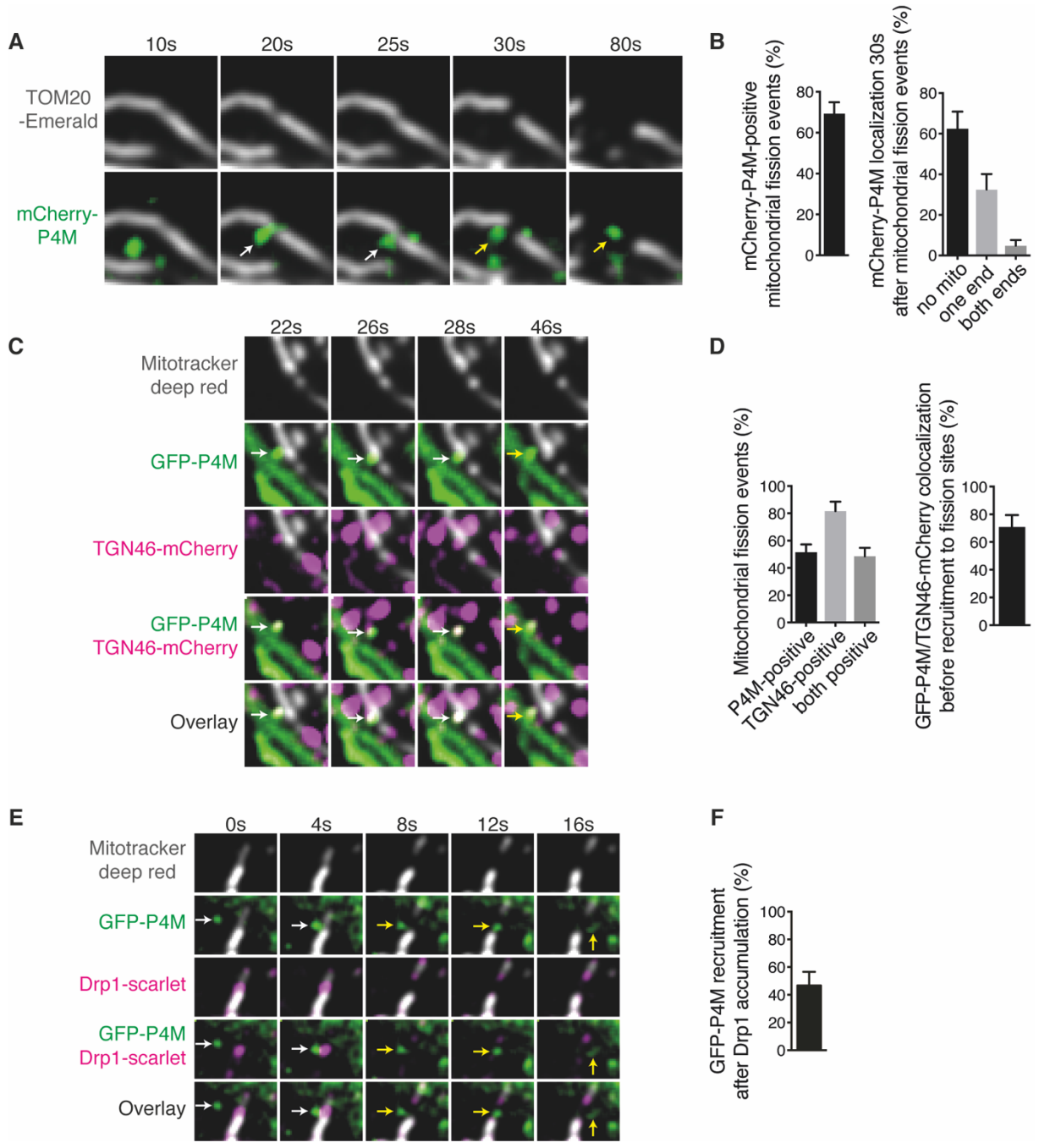

Fig. S14. mCherry/GFP-P4M is recruited to mitochondrial fission sites on TGN vesicles downstream of Drp1.

(A) Confocal time lapse imaging of HeLa cells transiently expressing mCherry-P4M and the mitochondrial marker TOM20-mEmerald. White and yellow arrows indicate mCherry-P4M puncta accumulating at constriction site just prior and after a fission event, respectively. **(B)** Quantification of mitochondrial fission events marked by mCherry-P4M prior division (left panel) and mCherry-P4M dynamics on mitochondria 30 sec after division (right panel). **(C)** Confocal time lapse imaging of HeLa cells transiently expressing GFP-P4M, TGN46-mCherry with mitochondria labelled using Mitotracker deep red. White and yellow arrows indicate GFP-P4M

puncta prior and after a fission event, respectively. **(D)** Quantification of mitochondrial fission events marked by GFP-P4M, TGN46-mCherry or double GFP-P4M/TGN46-mCherry prior division (left panel) and GFP-P4M/TGN46-mCherry dynamics before recruitment to mitochondrial division sites (right panel). **(E)** Confocal time lapse imaging of HeLa cells transiently expressing GFP-P4M, Drp1-Scarlet with mitochondria labelled using Mitotracker deep red. White and yellow arrows indicate GFP-P4M puncta prior and after a fission event, respectively. **(F)** Quantification of mitochondrial fission events marked by GFP-P4M downstream of Drp1-Scarlet recruitment. All values: mean ± SEM; at least three independent experiments.

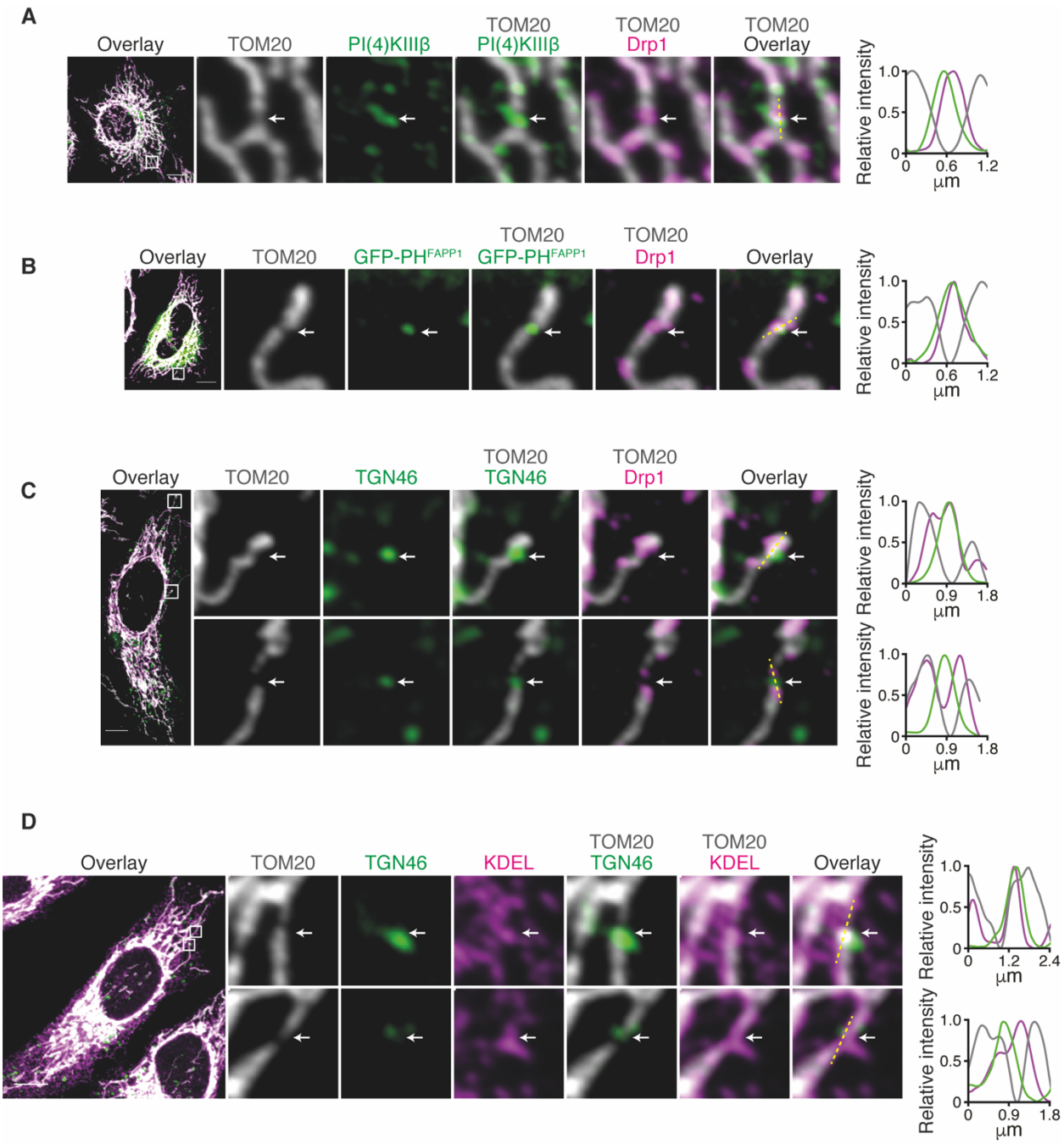

Fig. S15. PI(4)P pools on TGN-46 vesicles colocalize with Drp1 at ER-induced mitochondrial constriction.

(A-C) Representative confocal images of HeLa cells stained for **(A)** PI(4)KIIIβ, expressing **(B)** GFP-PH^{FAPP1}, and **(C)** TGN46-mCherry in combination to Drp1 and TOM20 labelling. White arrows indicate co-localization of PI(4)KIIIβ, GFP-PH^{FAPP1}, or TGN46-mCherry, with Drp1 at mitochondria. Line-scan analysis (right panels) of relative fluorescence intensity from the dashed line are shown. **(D)** Representative confocal images HeLa cells transfected with TGN46-mCherry showing TGN46-mCherry foci at mitochondrial constriction sites and ER contacts localization

(white arrows). Line-scan analysis (right panels) of relative fluorescence intensity from the dashed line are shown. All scale bars: 10 μm.

Captions for Movies S1-S16

Movie S1. Arf1-GFP is enriched at mitochondrial constriction sites before division.
HeLa cells transfected for 24 hr with Arf1-GFP (green) and TOM20-mCherry (white) were observed under ANDOR Dragonfly spinning disk confocal microscope using 100X objective and an sCMOS (Zyla) camera. 3 stacks of 0.3 μm each were acquired every 5 seconds. Images were then compiled by "max projection". Time-lapse images are shown in Figure 3C.

Movie S2. Additional example showing the Arf1-GFP accumulation at mitochondrial constriction sites before division.
HeLa cells transfected for 24 hr with Arf1-GFP (green) and TOM20-mCherry (white) were observed under ANDOR Dragonfly spinning disk confocal microscope using 100X objective and an EMCCD (iXon Ultra 888) camera. Images were acquired every 5 seconds.

Movie S3. Arf1-GFP accumulates at mitochondrial fission sites after Drp1-scarlet recruitment.
HeLa cells transfected for 24 hr with Arf1-GFP (green) and Drp1-scarlet (purple) and with mitochondria labelled with Mitotracker deep red FM (white) were observed under ANDOR Dragonfly spinning disk confocal microscope using 100X objective and an EMCCD (iXon Ultra 888) camera. Images were acquired every 2 seconds. Time-lapse images are shown in Figure 3E.

Movie S4. Arf1-GFP is enriched at mitochondria-ER contact sites before mitochondrial division.
HeLa cells transfected for 24 hr with Arf1-GFP (green) and ER-dsRED2 (purple) and with mitochondria labelled with Mitotracker deep red FM (white) were observed under ANDOR Dragonfly spinning disk confocal microscope using 100X objective and an EMCCD (iXon Ultra 888) camera. Images were acquired every 5 seconds. Time-lapse images are shown in Fig. S11D.

Movie S5. Additional example showing the Arf1-GFP localization at mitochondria-ER contacts before mitochondrial division.
HeLa cells transfected for 24 hr with Arf1-GFP (green) and ER-dsRED2 (purple) and with mitochondria labelled with Mitotracker deep red FM (white) were observed under ANDOR Dragonfly spinning disk confocal microscope using 100X objective and an EMCCD (iXon Ultra 888) camera. Images were acquired every 5 seconds.

Movie S6. Arf1-GFP is recruited at mitochondrial fission sites independently of LAMP1-mCherry.
HeLa cells transfected for 24 hr with Arf1-GFP (green) and LAMP1-mCherry (purple) and with mitochondria labelled with Mitotracker deep red FM (white) were observed under ANDOR Dragonfly spinning disk confocal microscope using 100X objective and an EMCCD (iXon Ultra 888) camera. Images were acquired every 2 seconds. Time-lapse images are shown in Figure 3G.

Movie S7. Arf1-GFP is recruited at mitochondrial fission sites with TGN46-mCherry.
HeLa cells transfected for 24 hr with Arf1-GFP (green) and TGN46-mCherry (purple) and with mitochondria labelled with Mitotracker deep red FM (white) were observed under ANDOR Dragonfly spinning disk confocal microscope using 100X objective and an EMCCD (iXon Ultra 888) camera. Images were acquired every 2 seconds. Time-lapse images are shown in Figure 3I.

Movie S8. PI(4)P builds up on mitochondrial constriction sites preceding mitochondrial division.
HeLa cells transfected for 24 hr with GFP-PH^{FAPP1} (green) and TOM20-mCherry (white) were observed under ANDOR Dragonfly spinning disk confocal microscope using 100X objective and an sCMOS (Zyla) camera. 3 stacks of 0.3 μm each were acquired every 5 seconds. Images were then compiled by "max projection". Time-lapse images are shown in Figure 4B.

Movie S9. Additional example showing the PI(4)P builds up on mitochondrial constriction sites preceding mitochondrial division.
HeLa cells transfected for 24 hr with GFP-PH^{FAPP1} (green) and TOM20-mCherry (white) were observed under ANDOR Dragonfly spinning disk confocal microscope using 100X objective and an sCMOS (Zyla) camera. 3 stacks of 0.3 μm each were acquired every 5 seconds. Images were then compiled by "max projection".

Movie S10. PI(4)P builds up on mitochondria-ER contacts preceding mitochondrial division.
HeLa cells transfected for 24 hr with GFP-PH^{FAPP1} (green) and ER-dsRed2 (purple) with mitochondria labelled with Mitotracker deep red FM (white) were observed under ANDOR Dragonfly spinning disk confocal microscope using 100X objective and an EMCCD (iXon Ultra 888) camera. Images were acquired every 5 seconds. Time-lapse images are shown in Fig. S13.

Movie S11. GFP-PH^{FAPP1} accumulates at mitochondrial fission sites after Drp1-scarlet recruitment.
HeLa cells transfected for 24 hr with GFP-PH^{FAPP1} (green) and Drp1-scarlet (purple) and with mitochondria labelled with Mitotracker deep red FM (white) were observed under ANDOR Dragonfly spinning disk confocal microscope using 100X objective and an EMCCD (iXon Ultra 888) camera. Images were acquired every 2 seconds. Time-lapse images are shown in Figure 4D.

Movie S12. GFP-PH^{FAPP1} is recruited at mitochondrial fission sites with TGN46-mCherry.
HeLa cells transfected for 24 hr with GFP-PH^{FAPP1} (green) and TGN46-mCherry (purple) and with mitochondria labelled with Mitotracker deep red FM (white) were observed under ANDOR Dragonfly spinning disk confocal microscope using 100X objective and an EMCCD (iXon Ultra 888) camera. Images were acquired every 2 seconds. Time-lapse images are shown in Figure 4F.

Movie S13. GFP-PH^{FAPP1} is recruited at mitochondrial fission sites independently of LAMP1-mCherry.
HeLa cells transfected for 24 hr with GFP-PH^{FAPP1} (green) and LAMP1-mCherry (purple) and with mitochondria labelled with Mitotracker deep red FM (white) were observed under ANDOR Dragonfly spinning disk confocal microscope using 100X objective and an EMCCD (iXon Ultra 888) camera. Images were acquired every 2 seconds. Time-lapse images are shown in Figure 4H.

Movie S14. PI(4)P builds up on mitochondrial constriction sites preceding mitochondrial division.
HeLa cells transfected for 24 hr with mCherry-P4M (green) and TOM20-mEmerald (white) were observed under ANDOR Dragonfly spinning disk confocal microscope using 100X objective and an EMCCD (iXon Ultra 888) camera. Images were acquired every 5 seconds. Time-lapse images are shown in Fig. S14A.

Movie S15. GFP-P4M is recruited to mitochondrial fission sites with TGN46-mCherry.
HeLa cells transfected for 24 hr with GFP-P4M (green) and TGN46-mCherry (purple) and with mitochondria labelled with Mitotracker deep red FM (white) were observed under ANDOR Dragonfly spinning disk confocal microscope using 100X objective and an EMCCD (iXon Ultra 888) camera. Images were acquired every 2 seconds. Time-lapse images are shown in Fig. S14C.

Movie S16. GFP-P4M accumulates at mitochondrial fission sites after Drp1-scarlet recruitment.
HeLa cells transfected for 24 hr with GFP-P4M (green) and Drp1-scarlet (purple) and with mitochondria labelled with Mitotracker deep red FM (white) were observed under ANDOR Dragonfly spinning disk confocal microscope using 100X objective and an EMCCD (iXon Ultra 888) camera. Images were acquired every 2 seconds. Time-lapse images are shown in Fig. S14E.